Monthly Notices of the ROYAL ASTRONOMICAL SOCIETY

MNRAS **512,** 2556–2572 (2022) https://doi.org/10.1093/mnras/stac634
Advance Access publication 2022 March 10

Gas inflows in the polar ring of NGC 4111: the birth of an AGN

Gabriel R. Hauschild Roier [1★] Thaisa Storchi-Bergmann,[1★] Richard M. McDermid,[2] Jonelle L. Walsh,[3] Joanne Tan,[3] Jonathan Cohn,[3] Davor Krajnovic,[4] Jenny Greene,[5] Monica Valluri,[6] Kayhan Gültekin,[6] Sabine Thater,[7] Glenn van de Ven [7] Karl Gebhardt,[8] Nora Lützgendorf,[9] Benjamin D. Boizelle,[3,10] Chung-Pei Ma[11] and Aaron J. Barth [12]

[1]*Instituto de Física, Universidade Federal do Rio Grande do Sul, Av. Bento Gonçalves 9500, 91501-970, Porto Alegre, RS, Brazil*
[2]*Astronomy, Astrophysics, and Astrophotonics Research Centre, Department of Physics and Astronomy, Macquarie University, NSW 2109, Australia*
[3]*George P. and Cynthia W. Mitchell Institute for Fundamental Physics and Astronomy, Texas A&M University, 4242 TAMU, College Station, TX 77843, USA*
[4]*Leibniz Institute for Astrophysics, Potsdam 14482, Germany*
[5]*Department of Astrophysical Sciences, Princeton University, NJ 08544, USA*
[6]*Department of Astronomy, University of Michigan, Ann Arbor, MI 48109, USA*
[7]*Department of Astronomy, University of Vienna, Vienna 1180, Austria*
[8]*Department of Astronomy, University of Texas at Austin, Austin, TX 78712-1205, USA*
[9]*European Space Agency, c/o STScI, 3700 San Martin Drive, Baltimore, MD 21218, USA*
[10]*Department of Physics and Astronomy, N283 ESC, Brigham Young University, Provo, UT 84602, USA*
[11]*Department of Astronomy, UC Berkeley, CA 94720-3411, USA*
[12]*Department of Physics and Astronomy, 4129 Frederick Reines Hall, University of California, Irvine, CA 92697, USA*

Accepted 2022 March 2. Received 2022 February 9; in original form 2021 October 20

ABSTRACT

We have used *Hubble Space Telescope* (*HST*) images, SAURON Integral Field Spectroscopy (IFS), and adaptative optics assisted Gemini NIFS near-infrared K-band IFS to map the stellar and gas distribution, excitation and kinematics of the inner few kpc of the nearby edge-on S0 galaxy NGC 4111. The *HST* images map its ≈450 pc diameter dusty polar ring, with an estimated gas mass $\geq 10^7$ $M_\odot$. The NIFS data cube maps the inner 110 pc radius at ≈7 pc spatial resolution, revealing a ≈220 pc diameter polar ring in hot (2267 ± 166 K) molecular H_2 1–0 S(1) gas embedded in the polar ring. The stellar velocity field shows disc-dominated kinematics along the galaxy plane both in the SAURON large scale and in the NIFS nuclear-scale data. The large-scale [O III] λ5007 Å velocity field shows a superposition of two disc kinematics: one similar to that of the stars and another along the polar ring, showing non-circular motions that seem to connect with the velocity field of the nuclear H_2 ring, whose kinematics indicate accelerated inflow to the nucleus. The estimated mass inflow rate is enough not only to feed an active galactic nucleus (AGN) but also to trigger circumnuclear star formation in the near future. We propose a scenario in which gas from the polar ring, which probably originated from the capture of a dwarf galaxy, is moving inwards and triggering an AGN, as supported by the local X-ray emission, which seems to be the source of the H_2 1–0 S(1) excitation. The fact that we see neither near-UV nor Br γ emission suggests that the nascent AGN is still deeply buried under the optically thick dust of the polar ring.

Key words: galaxies: active – galaxies: individual: NGC 4111 – galaxies: kinematics and dynamics – galaxies: nuclei.

1 INTRODUCTION

Interactions between galaxies impact their evolution and that of their central supermassive black holes (SMBHs), triggering episodes of star formation and nuclear activity. Major mergers seem to be the dominant process of SMBH growth at large SMBH masses ($\geq 10^8$ $M_\odot$), triggering luminous active galactic nuclei (AGNs), while at lower AGN luminosities ($\leq 10^{44}$ erg s^{-1}), the most probable triggers are minor mergers and secular processes driving inflows towards the nucleus such as gravitational torques in nuclear spirals and bars (Storchi-Bergmann & Schnorr-Müller 2019, and references therein). Minor mergers are frequent in dense galactic environments, when massive early-type galaxies capture gas-rich dwarf galaxies that replenish the inner region of the galaxy with gas, leading to episodes of renewed star formation and/or the triggering of nuclear activity (e.g. Neistein & Netzer 2014).

Such a minor merger may have recently happened in the nearby SO edge-on galaxy NGC 4111, known to host an extended H I envelope (Wolfinger et al. 2013). A member of the Ursa Major galaxy group, this galaxy lies at a distance of 15.1 Mpc [according to the NASA Extragalactic Database (NED),[1] using a Lambda cold dark matter (ΛCDM) cosmology with $H_0 = 67.8$ km s^{-1} Mpc^{-1}, $\Omega_m = 0.308$, and $\Omega_\Lambda = 0.692$] – for which 1 arcsec corresponds to 73.1 pc. NGC 4111 has at least four companion galaxies located within 250 kpc from it, with the nearest only 30–40 kpc away (Karachentsev, Nasonova & Courtois 2013; Pak et al. 2014; Kasparova et al. 2016). NGC 4111 has

★ E-mail: gabriel.roier@ufrgs.br (GRHR); thaisa@ufrgs.br (TSB)

[1]https://ned.ipac.caltech.edu/

a dust structure crossing the nucleus perpendicular to the galaxy disc (Barth et al. 1998) associated with H I filaments, which suggest an origin from tidal stripping of gas from a nearby or recently captured galaxy (Verheijen & Zwaan 2001; Verheijen 2004; Pak et al. 2014).

Kasparova et al. (2016) showed that NGC 4111 has a flat stellar age distribution of ∼5 Gyr across most of its disc. In the inner region, however, with galaxy mid-plane distance of ∼700 pc, single stellar population modelling reveals a more metal-rich and younger stellar population with a characteristic 4 Gyr age. This very flattened young stellar component could be due to a previous gas-rich minor merger.

NGC 4111 was identified as an AGN by González-Martín et al. (2009), using *Chandra* X-ray data. In that work, the column density of H I and H_2 were calculated to be 4.67×10^{22} cm^{-2} and 37.71×10^{22} cm^{-2}, respectively. NGC 4111 images from *Chandra* show extended soft X-ray emission and nuclear-only hard emission, with luminosities measured as $\log(L_{\rm soft}) = 40.9$ erg s^{-1} (0.5–2.0 keV) and $\log(L_{\rm hard}) = 40.4$ erg s^{-1} (2.0–10.0 keV). This suggests that the source of high-energy X-rays is a fairly obscured AGN which is embedded in the dense dust ring, while the soft emission is spread across the galaxy plane and has a maximum in the central region. This is also supported by the fact that near-UV emission from the nucleus is not detected in *HST* images (Barth et al. 1998). NGC 4111 shows 5 GHz radio emission extended by 110.4 pc × 72.2 pc and position angle of 29 ± 11° according to Nyland et al. (2016); however, the origin of the radio emission is unclear and the nucleus of the galaxy is classified as a LINER (Ho, Filippenko & Sargent 1997).

NGC 4111 was observed with the Gemini Near-Infrared Spectrograph (NIFS) as part of the project 'Addressing a Bias in the Relation Between Galaxies and Their Central Black Holes' (P.I. Jonelle Walsh). While the main goal of the project is to determine SMBH masses from the stellar kinematics in nearby galaxies, the NIFS *K*-band observations of NGC 4111 revealed many lines of hot molecular H_2 gas emission in the spectra. These lines reveal peculiar excitation and kinematics that deserve a study of its own. The goal of this paper is to investigate the nature of the excitation and kinematics of the hot H_2 gas emission of the inner ≈100 pc of the galaxy. In order to do this, we also employed *Hubble Space Telescope* (*HST*) images and large-scale integral field data from the Spectrographic Areal Unit for Research on Optical Nebulae survey (SAURON).

This paper is organized as follows. In Section 2, we present the observations and data reduction. In Section 3, we present the measurements for the *HST* (regarding the photometry), SAURON, and NIFS data (regarding the emission lines fitting and kinematics, and the stellar kinematics). In Section 4, we present our results and discussion for all three instruments, so that in Section 5 we compare these results and propose a scenario for the observational evidences of NGC 4111. Finally, in Section 6 we present our conclusions.

2 OBSERVATIONS

As a part of GO-15323 (PI: Jonelle Walsh), we obtained *HST* Wide Field Camera 3 (WFC3) imaging in the F475W (see Fig. 1) and F160W filters. The F160W data were obtained using the RAPID sequence in a two-point WFC3-IR-DITHER-LINE pattern, with a total 53 s exposure time. The F475W data were obtained in an ideal four-point dither pattern using only the UVIS2-2K2C-SUB aperture, with a total 920 s exposure time. The WFC3 data were combined into separate F475W and F160W mosaics with the same origin and pixel scale using `AstroDrizzle` (Gonzaga et al. 2012).

K-band spectroscopy of the nuclear region of NGC 4111 was obtained using the instrument NIFS – Near-Infrared Integral Field Spectrograph (McGregor et al. 2003), with the adaptive optics module Altair (Herriot et al. 2000; Boccas et al. 2006) at the Gemini North Telescope on 2019 May 9. We acquired 600 s exposures following an object-sky-object sequence, with a total on-source time of 1 hr via the program GN-2019A-LP-8 (P.I. Jonelle Walsh). We used the $H + K$ filter and K grating centred on 2.20 μm, which provided coverage of 1.99 μm–2.40 μm with $R \sim 5290$. NIFS is an image slicer with a Field-of-View (FoV) of 3 arcsec × 3 arcsec – corresponding to 219 × 219 pc^2 at the galaxy, sampled with pixels of 0.04 arcsec × 0.1 arcsec; the observations with the adaptative optics module Altair delivered data with a point spread function (PSF) – as determined from the spatial profiles of standard stars – FWHM of 0.1 arcsec corresponding to a spatial resolution of ≈7 pc at NGC 4111. We reduced the NIFS data using IRAF tasks (Tody 1986, 1993) within the Gemini package v1.14, in combination with PYTHON scripts we developed[2] based on the example NIFS processing scripts.[3] The main steps included sky subtraction, flat-fielding, cosmic ray cleaning and bad pixel removal, wavelength calibration, and spatial rectification. The galaxy spectra were telluric corrected using an A0 V star (HD95126 or HD116405), after removal of the Br γ absorption line and the blackbody continuum. We constructed a temporary data cube for each galaxy exposure and collapsed the cubes to determine the spatial offsets by means of a two-dimensional cross-correlation. Then all six of the galaxy frames were interpolated on to a single data cube with 0.05 arcsec versus 0.05 arcsec spaxels and wavelength sampling of 2.13 Å. Finally, a rough flux calibration was carried out using the telluric-corrected HD116405 spectrum and comparing the flux density at the isophotal wavelength of the Two Micron All Sky Survey (2MASS) *Ks* filter to the 2MASS magnitude reported in the SIMBAD astronomical data base (Wenger et al. 2000). This conversion was applied to the final

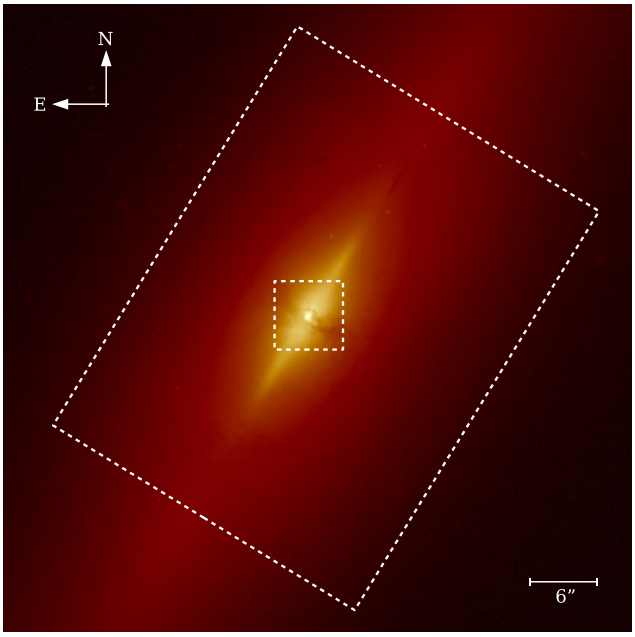

Figure 1. *HST* large-scale image of NGC 4111 in the F475W filter, covering a 4.8 kpc×4.8 kpc region. The white dashed-line rectangle shows the 31 arcsec × 41 arcsec SAURON FoV and the smaller white dashed-line square delimits a 6 arcsec × 6 arcsec region containing the dusty polar ring shown in the colour map of Fig. 2. North is up and east is left.

[2] https://github.com/jlwalsh12/NIFS-reduction-pipeline
[3] https://www.gemini.edu/instrumentation/nifs/data-reduction

NGC 4111 data cube, resulting in calibrated units of erg s^{-1} cm^{-2} $Å^{-1}$. We reduced the sky frames in a similar manner, but subtracted a 600 s master dark frame. We applied the same spatial offsets as the ones used for the galaxy frames to produce a single sky cube and measured the line spread function over the NIFS FoV from 13 strong, isolated sky lines. The sky lines spectral resolution varies over the NIFS FoV, ranging from an FWHM of 3.5 to 5.9 Å, with an FWHM median resolution of 3.9 Å.

Optical integral field spectroscopy (IFS) data were obtained with the SAURON instrument (Bacon et al. 2001) on the William Herschel Telescope, La Palma as part of the ATLAS^{3D} Survey (Cappellari et al. 2011). SAURON provides a 31 arcsec × 41 arcsec FoV – corresponding to 2.3 kpc × 3.0 kpc at the galaxy, sampled with 0.94 arcsec square lenslets, and with a spectral resolution of 4.2 Å FWHM ($\sigma_{\rm inst}$ = 105 km s^{-1}), covering the wavelength range of 4800–5380 Å. The observations comprised the combination of two exposures of 30 minutes, obtained on UT 2007 April 20, together with associated calibrations. The data were reduced via standard procedures using the dedicated XSAURON software package (Bacon et al. 2001; Emsellem et al. 2004). The approximate seeing FWHM was 1.2 arcsec, corresponding to a spatial resolution of ≈88 pc at the galaxy. These reduced spectral data cubes are publicly available at www.purl.org/atlas3d.

The aforementioned data were astrometrically matched using the WCS data in the headers, followed by a visual inspection to assure the correct relative position of the images.

3 MEASUREMENTS

3.1 *HST*

Fig. 1 shows the *HST* F475W continuum image with the 31 arcsec × 41 arcsec SAURON FoV delineated by a white dashed-line rectangle. This image shows the edge-on orientation of the galaxy and the dusty polar ring crossing the nucleus approximately perpendicular to the disc of the galaxy. The 6 arcsec × 6 arcsec white dashed-line square encloses the region where the dusty polar ring is observed.

Using the F475W and the F160W images, we built the F475W–F160W colour map, with the inner 6 arcsec × 6 arcsec region shown in Fig. 2. This map shows that the dusty ring has a diameter of ≈450 pc (6.3 arcsec) and a width of ≈130 pc (1.8 arcsec). The 3 arcsec × 3 arcsec dashed white square in this figure shows the NIFS FoV, while the *white* contours delineates the flux distribution in the H_2(1–0) S(1) λ 2.1218 μm emission line that has the shape of an off-centred inclined ring, as shown and discussed in the following section (see Fig. 5).

3.2 SAURON

The SAURON optical spectra were analysed first by using Voronoi binning (Cappellari & Copin 2003) to increase the SNR of the spectra. We adopted a lower threshold of SNR = 40 and ran the PPXF code (Cappellari & Emsellem 2004) on the binned spaxels to measure the stellar kinematics. PPXF uses a stellar spectral base to fit the absorption lines in the galaxy spectrum in order to measure the kinematics (velocity, velocity dispersion, and the h_3 and h_4 Gauss–Hermite polynomials coefficients) in these lines. In this work, we used the MILES stellar templates (Falcón-Barroso et al. 2011) as a base for PPXF. Emission line properties were extracted using an implementation of the GANDALF (Gas AND Absorption Line Fitting) software (Sarzi et al. 2017). In this implementation, the previously derived PPXF stellar kinematics are fixed, and MILES SSP

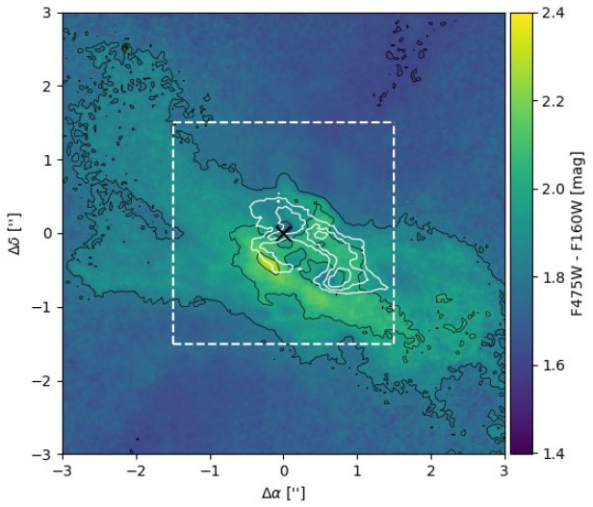

Figure 2. *HST* F475W – F160W colour map within the inner 6 arcsec × 6 arcsec (440 × 440 pc^2 at NGC 4111). Overplotted in white are the contours from the H_2λ2.1218 μm emission line flux distribution (see Section 3.3), and in black a cross shows the location of the peak of the stellar *K*-band continuum from NIFS, adopted as corresponding to the galaxy nucleus. The white dashed lines demarcate the NIFS FoV.

model templates are broadened by the corresponding LOSVD. The template weights are permitted to vary, together with the parameters of single Gaussian emission-line components. The [O III]λλ4959, 5007 doublet is initially fitted, as this is generally the most easily detected line without strong coincident absorption features. This fixes the emission-line kinematics for a second pass, where an H β emission component is also included. The fitted emission line is considered a secure detection if it has an amplitude four times higher than the local noise level, otherwise it is ignored.

3.3 NIFS

Sample spectra from NIFS are shown in Fig. 3, integrated within 0.1 arcsec × 01 arcsec windows, corresponding to the nucleus (labelled *X* in Fig. 5) and two extranuclear regions: one from a position over the H_2 off-centred ring (labelled *B* in Fig. 5) and from a region beyond this ring at 1.25 arcsec (91 pc) from the nucleus (labelled *C* in Fig. 5), comprising mostly light from the stellar component of the galaxy. The spectra show absorption lines from the stellar population, and H_2 emission lines from hot molecular gas. Fig. 3 identifies the wavelengths of the H_2 emission lines as well as that of the Br γ line, which is not present in the spectra. We note that the H_2 emission is observed only along the off-centred ring above and that the Br γ line is absent over the whole area covered by the NIFS FoV (see Section 4.3.2).

In order to measure the properties of the emitting H_2 gas in the NIFS data cube, we used the latest version (v1.1) of the software IFSCube (Ruschel-Dutra & Oliveira 2020) to fit the emission lines profiles with Gauss–Hermite polynomials, within the 21180–21280 Å spectral window (in observed wavelengths), which encompasses the H_2 λ2.1218 μm emission line and a continuum region. IFSCube fits a polynomial component to the continuum adjacent to the line, whose degree can be chosen during the fit. We opted by the use of a linear function, that fitted well the continuum in all spaxels. In Fig. 4, we present example fits from IFSCube for two spectra extracted in windows of 0.1 arcsec × 0.1 arcsec, one from the nucleus and the other from a position along the molecular H_2 ring

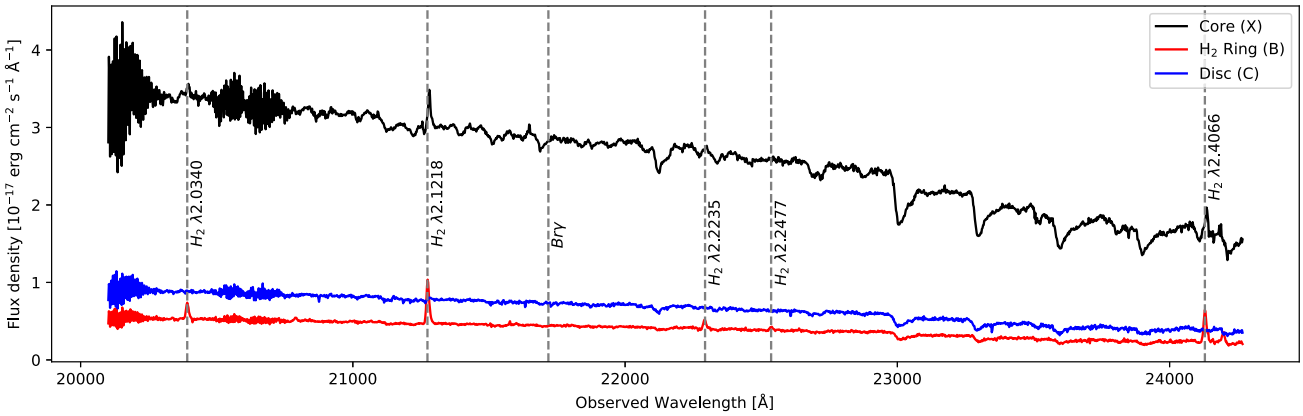

Figure 3. NIFS spectra in observed wavelength from three representative regions of the galaxy, integrated within apertures of 0.1 arcsec × 0.1 arcsec: nuclear spectrum in black; H_2 ring region spectrum in red, extracted from position *B* in Fig. 5; spectrum from the disc of the galaxy in blue, extracted from position *C* in Fig. 5. The wavelengths of the H_2 emission lines are marked with dashed grey lines, along with that of the absent Br γ line.

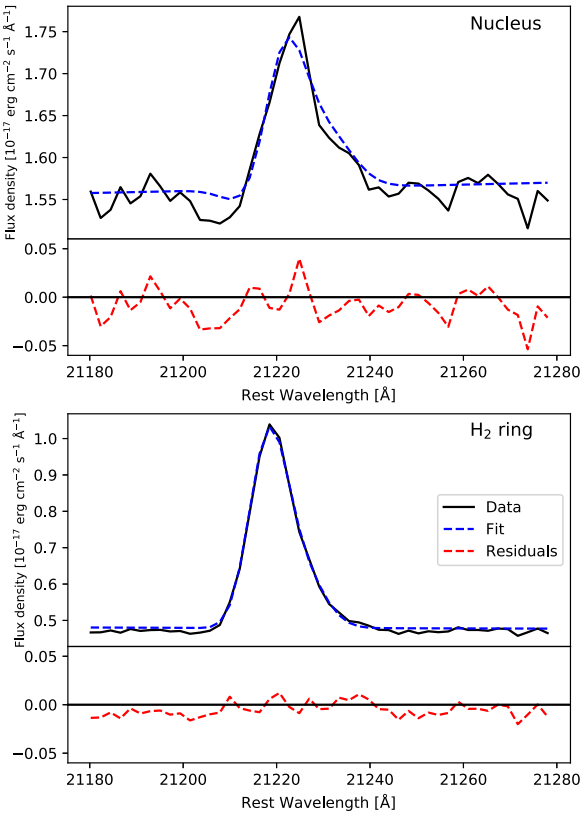

Figure 4. The fit of the $H_2\lambda2.1218$ µm emission-line profile at the nucleus and position B in the ring (see Fig. 5). The rest profile is shown in black lines and the IFSCube Gauss–Hermite polynomial fit in blue dashed lines, while the residuals are shown in red dashed lines.

(position B in Fig. 5), showing in black lines the spectra, in dashed blue lines the fit and in dashed red lines the residuals. We imposed a lower threshold for the signal-to-noise ratio (SNR) as obtained from the ratio between the peak of the line and the noise in the continuum adjacent to the line (standard deviation of the continuum). Spaxels with a SNR less than 2 are regarded as noise and excluded from the fit. This same noise was used to apply the Monte Carlo technique in order to evaluate the errors in the parameters resulting from the

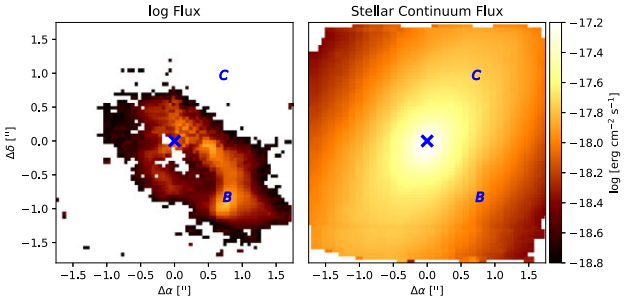

Figure 5. Left: Integrated flux distribution in the molecular H_2(1–0) S(1) $\lambda2.1218\,\mu$m emission line. Right: Stellar continuum flux distribution from the NIFS data cube, obtained by integrating the spectra within the 2.175–2.200 µm wavelength range. The cross shows the spaxel with the highest integrated continuum flux – identified with the galaxy nucleus; the letters B and C identify the locations from where the spectra identified in Fig. 3 were extracted.

fit. The left-hand panel of Fig. 5 shows the resulting flux map of the H_2 $\lambda2.1218$ µm emission line, resembling a tilted ring oriented approximately perpendicular to the galaxy plane. The right-hand panel shows the flux distribution of the stellar continuum, integrated in a window covering the 2.175–2.200 µm wavelength range. In Fig. 5, we also identify the nucleus and the other locations where the spectra from Fig. 3 were extracted.

We also obtained the stellar kinematics using a similar approach to that used for the SAURON data (see Section 3.2): first we used Voronoi binning to increase the SNR of the spectra until it reached a lower threshold of SNR = 50 in the stellar continuum and then executed pPXF with the Winge stellar templates (Winge, Riffel & Storchi-Bergmann 2009) as a base. The stellar kinematics fits at positions *X*, *B,* and *C* of Fig. 5, are shown, from top to bottom, in Fig. 6, where the normalized spectra are shown in black, the fit in blue and the residuals in red.

4 RESULTS AND DISCUSSION

4.1 Galactic scale – *HST*

The F475W-F160W colour map of Fig. 2 traces the obscuring structure crossing the nuclear region seen in Fig. 1, mapping its reddening and revealing the polar ring dust distribution which

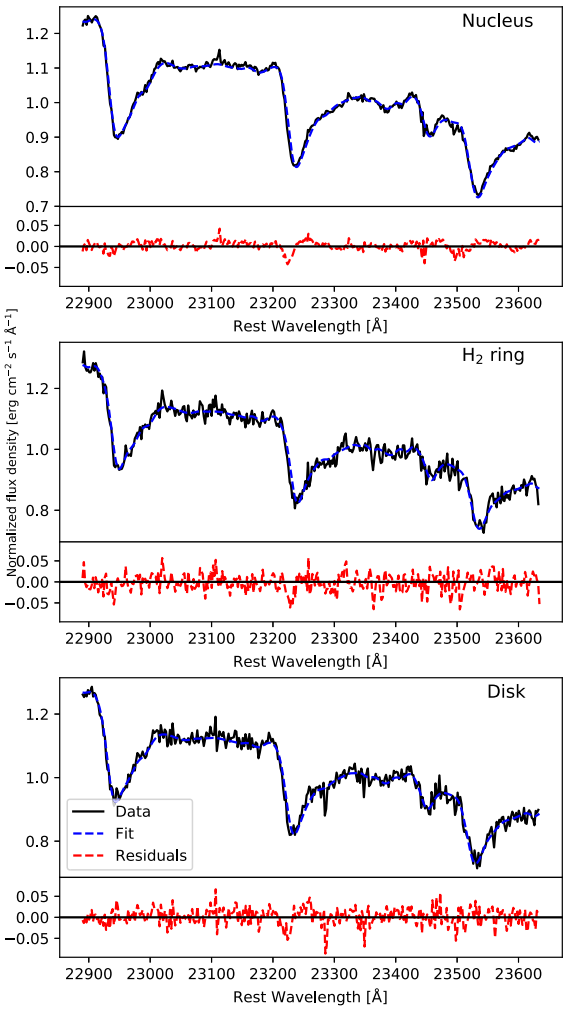

Figure 6. The fit of the stellar kinematics with pPXF was performed in the spectral range of 22950–23700 Å (in observed wavelengths). The figure shows three representative Voronoi-binned spectra in black, from the nucleus and positions B and C in Fig. 5, together with the fits in blue and residuals in red.

is extended perpendicular to the galaxy plane by approximately ≈450 pc and shows the reddest colours in an off-centred ring with a major axis of ≈200 pc. The NIFS FoV is identified via the dashed white square. We have overplotted on Fig. 2, contours from the NIFS H_2 λ2.1218 μm flux map of Fig. 5 shown in white, while the location of the peak flux of the stellar continuum (adopted as the galaxy nucleus) is shown as a black cross. This figure shows that the H_2 ring is spatially associated with the off-centred ring with the reddest colours in the polar ring that can be attributed to increased reddening by dust. This colour map reveals that the molecular hydrogen emission is *de facto* related to the dust, with both presenting similar off-centred ring-like structure.

4.1.1 Cold gas mass

We have used the colour map of Fig. 2 to obtain the extinction of the region under the assumption that the intrinsic colour of the stellar population is that of the galaxy disc, adopted as F475W–F160W = 1.5, according to Fig. 2, and considering the dust obscuration as due to a foreground obscuring screen. Fig. A1 of the Appendix shows the resulting $A_{F475W} - A_{F160W}$ extinction map of the inner 6.0 arcsec × 6.0 arcsec that has an excess extinction at ≈4750 Å relative to ≈ 1.6 μm of up to ∼ 0.8 mag in the ring relative to the stellar population. This extinction is consistent with the relatively high column density measured by González-Martín et al. (2009) in the *Chandra* observations.

In our calculation, we have assumed that the dust is a foreground screen obscuring the light from the galaxy, and we have used the extinction law from Savage & Mathis (1979) in order to derive the extinction values $E(B-V)$ from the $A_{F475W} - A_{F160W}$ extinction map, with $A_\lambda/E(B-V)$ values obtained from the last column of table 2 of Savage & Mathis (1979). Also following Savage & Mathis (1979), we used the $E(B-V)$ values derived from the extinction map of Fig. A1 and a gas-to-colour excess of $\langle N(\mathrm{H\,I} + \mathrm{H_2})/E(B-V)\rangle = 5.8 \times 10^{21}$ atoms cm^{-2} mag^{-1} in order to obtain a lower limit for the gas mass in each spaxel. Multiplying by the mass of the proton and dividing by the area of each spaxel in units of pc^2, we obtain the surface gas mass distribution shown in Fig. A2 of the Appendix. Adding the mass values of all spaxels, the resulting lower limit for the cold gas mass in the 450 pc polar ring is $M_{gas} = 9.8 \times 10^6$ M$_\odot$.

4.2 Galactic scale – SAURON

4.2.1 Stellar and ionized gas flux distributions

Flux distributions in the optical continuum, [O III]λ5007 and H β gas emission lines over the inner ≈20 arcsec of the galaxy obtained from the SAURON observations are shown in Fig. 7. In the continuum (mapping the optical stellar component), the flux distribution is brightest at the nucleus decreasing almost uniformly in all directions except for a slightly more abrupt decrease to the NW than to the SE. At faint levels there is some extension along the galaxy plane. The flux distributions in the emission lines are similar to that in the continuum for the highest flux levels around the nucleus but show also more emission outwards, in particular to the SW towards the border of the FoV.

The rightmost panel of Fig. 7 shows that the line flux maps of the [O III]λ5007 and H β lines from the SAURON data produce a line ratio map with values in the range $1 \leq F[\mathrm{O\,III}]/F(\mathrm{H}\,\beta) \leq 3$, increasing towards the borders of the FoV. As the SAURON data does not cover the H α spectral region, we use a spectrum from this region from Ho, Filippenko & Sargent (1995) who find [F([N II]λ6584)/F(H α) ≈1, which puts NGC 4111 in the LINER region of the BPT diagram (Baldwin, Phillips & Terlevich 1981; Kewley et al. 2001; Kauffmann et al. 2003; Cid Fernandes et al. 2010), in agreement with the classification from Nyland et al. (2016).

4.2.2 Stellar kinematics

The SAURON data kinematics is shown in Fig. 8. The right-hand panels show the stellar kinematics on kpc scales. The top panel shows a rotation pattern with redshifts to the SE and blueshifts to the NW.

The large-scale stellar velocity field obtained from the SAURON data was previously analysed by Krajnovic et al. (2011), who concluded that it presents ordered and disc-like rotation, with a kinematic position angle of 149.5 deg ±2.2. The stellar velocity dispersion $\sigma_\star$ shown in the bottom right-hand panel, presents a small decrease in a linear structure, extended by ≈800 pc crossing the galaxy bulge along the major axis of the galaxy. This feature suggests the presence of a colder structure – as compared to the galaxy bulge, such as a disc of stars rotating in the galaxy plane that may have formed from recently acquired gas. Indeed, stellar population properties measured via line-strength indices and spectral

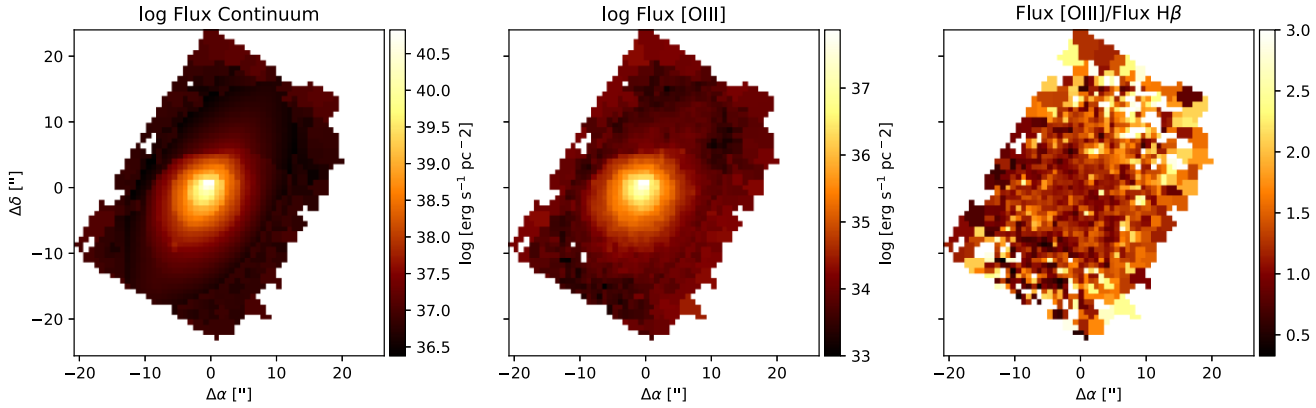

Figure 7. From left to right: Flux surface density distributions in the optical continuum, [O III]λ5007, and the line ratio map [O III]/H β obtained from the SAURON data.

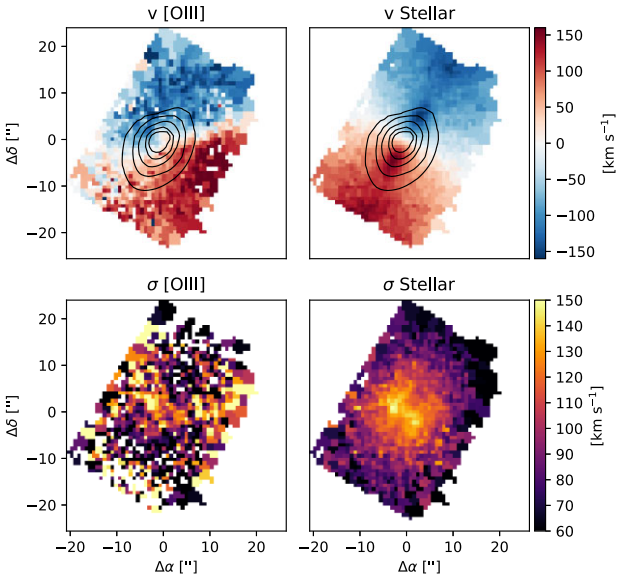

Figure 8. Kinematics from SAURON data. Top: Ionized gas and stellar velocity field (centroid velocity v), with contour lines from the SAURON continuum flux from Fig. 7. Bottom: gas and stellar velocity dispersion σ.

fitting of this data by McDermid et al. (2015) reveal the presence of younger stars than that of the surrounding bulge in this region, what is also consistent with the stellar age of the region obtained by Kasparova et al. (2016).

4.2.3 *Ionized gas kinematics*

The [O III] ionized gas kinematics probed by SAURON on kpc scales is shown in the left-hand panels of Fig. 8. The ionized gas velocity field v[O III] shown in the top panel presents a different orientation from that of the stellar component, with redshifts to the S-SW and blueshifts to the N-NE. As compared with the stellar velocity field, it presents a $\approx$50° shift in the orientation of the apparent kinematic major axis from the $\approx$150° (PA east of North of the redshifted side) of the stellar kinematics, bringing the PA of the gas velocity field to $\approx$200°.

Furthermore, the ionized gas velocity dispersion map shows the highest values at various non-central locations. In particular, they seem to be observed mostly along the minor-axis, although not exactly and with a bend towards N on both the E and W sides of the galaxy.

4.2.4 *Kinemetric analysis*

In order to try to quantify the kinematic properties described above, we analyse the SAURON stellar and gaseous velocity maps using kinemetry (Krajnovic et al. 2006). This method searches for the best-fitting ellipses (specified by the position angle PA and the ellipse flattening Q) along that the velocities can be described as a function of a cosine change in the eccentric anomaly. Kinemetry is built on the assumption that the velocities along the ellipses can be parametrized by $V = V_{\rm rot}\cos(\theta)$, where $V_{\rm rot}$ is the amplitude of rotation and θ is the eccentric anomaly.

Kinemetry performs an harmonic decomposition of velocities along ellipses and determines the properties of the best-fitting ellipse by minimizing the Fourier coefficients in a truncated Fourier Series, summing over the odd values of n: $V(r,\theta) = V_0 + \sum_{n=1}^{3}[a_n(r)\sin(n\theta) + b_n(r)\cos(n\theta)]$, except for b_1 (from here on called $V_{\rm rot}$). V_0 is the systemic velocity, θ is the eccentric anomaly, and $a_n(r)$ and $b_n(r)$ are the amplitudes at a given radial distance r. Therefore, the products of the kinemetry analysis are the kinematic PA and flattening (Q) of the best-fitting ellipses along a set of radii, $V_{\rm rot}$, and higher harmonic terms that describe the variation of the velocities along the ellipse.

The assumption behind kinemetry is that the motion of gas clouds follow circular orbits in a thin (inclined) disc (e.g. Schoenmakers, Franx & de Zeeuw 1997; Wong, Blitz & Bosma 2004; van de Ven & Fathi 2010). Therefore, the dominant kinemetry term, the one next to the cos (θ) harmonics, is $V_{\rm rot} = V_{\rm circ}$, which characterizes the circular motions in the disc. In case gas clouds are not moving on circular orbits (i.e. due to turbulence or non-settled nature of the disc), the PA and Q describing the ellipse will vary with radius. The variation of PA and Q can be related to the structural changes of the disc, which comprises rings of different orientations and inclinations. A further effect is the non-negligible higher harmonic coefficients beyond b_1. A similar principle applies for the stellar orbits in thin discs, but the majority of early-type galaxies actually show regular disc-like kinematics (Krajnovic et al. 2008, 2011).

As pointed out previously, the SAURON stellar velocity map of NGC 4111 was already analysed by Krajnovic et al. (2011), who concluded that the stellar rotation is indeed ordered and disc like.

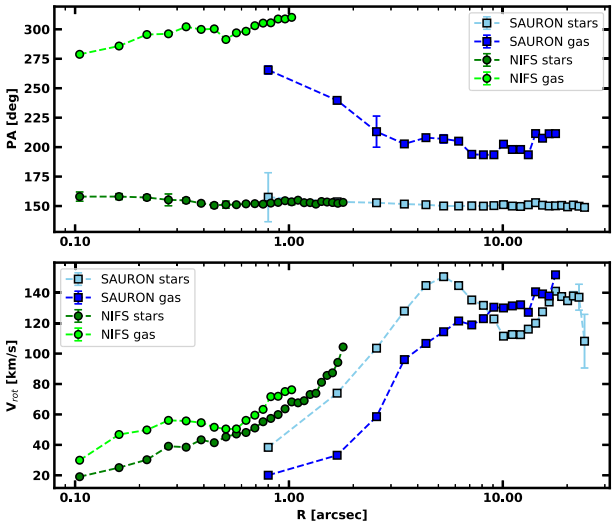

Figure 9. Position angle (top) and rotational velocity (bottom) of the SAURON and NIFS stellar and gas velocity maps as derived with kinemetry. Results for the SAURON kinematics are shown with light-blue and blue squares (stars and gas, respectively), and for the NIFS kinematics with green an lime circles (stars and gas, respectively).

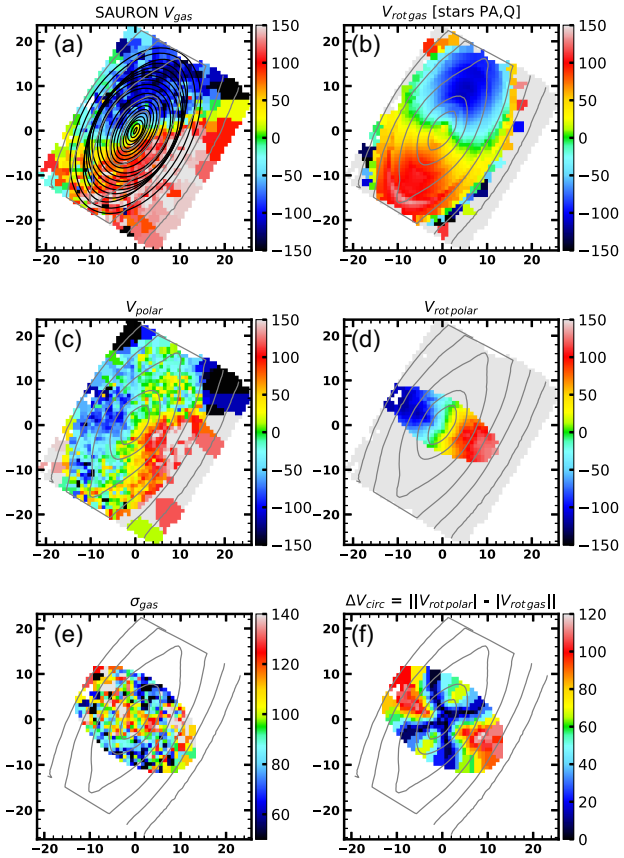

Figure 10. Analysis of the polar motions of the SAURON ionized gas. Panel (a): The SAURON gas velocity field as in Fig. 8, with overplotted ellipses used to extract the gas motions in the equatorial plane of the galaxy. Panel (b): Resulting velocity field of the gas in the equatorial plane of the galaxy. Panel (c): The velocity field representing 'polar' motions of the ionized gas, obtained by subtracting velocity field in panel b) (ordered rotation of the gas in the equatorial plane of the galaxy) from the SAURON gas velocity field in panel a). Panel (d): Ordered motion of the gas in the polar disc, obtained using kinemetry. Panel (e): SAURON gas velocity dispersion map as in Fig. 8, but limited to the same region as in panel (d), where there are data from the polar motions. Panel (f): Absolute difference between the ordered motions in the equatorial and the polar planes (panels b and d). Note that panels (e) and (f) have high-velocity values in the same regions, providing a qualitative explanation for the unusual structure of the SAURON gas velocity dispersion map. Note also that the colour bars on these panels are not the same, but adjusted to highlight the kinematic features. On all panels, grey lines present the isophotes of the stellar light.

Here, we repeat this analysis to extend it to the SAURON gas to quantify how regular gas motions are. In Fig. 9, we show the variation of the position angles of best-fitting ellipses, as well as the variation of $V_{\rm rot}$. While running kinemetry on the gas velocity maps, the flattening of the ellipses was poorly constrained. Therefore, we imposed a limit on the range of possible $Q > 0.98$, making ellipses close to circles. In this way, we were still able to recover robust estimates for the PA and $V_{\rm rot}$. Also shown in this figure are the kinemetry results from the NIFS data to be discussed in Section 4.3.6.

As pointed out above, the visual inspection of the SAURON gas velocity map already shows (see Fig. 8), a significant difference in the orientation of gas and stellar kinematics. This difference is now quantified by kinemetry to be about 55° beyond the inner ≈3 arcsec. This angle for the gas kinematics does not coincide with any of the principal axes in NGC 4111 (the kinematic and photometric major axes have the same orientation within errors), and, therefore, the [O III] emission line gas is in an unstable configuration. Not only is the gas kinematics misaligned with respect to that of the stars, but there seems to be a continuous twisting of the kinematic position angle towards the nucleus. This change of the gas kinematics position angle suggests the presence of non-circular motions of gas clouds.

The pattern in the gas velocity dispersion (the bottom panel of Fig. 8) with increased values in a twisted configuration could be indication of kinematic disturbance in the gas due to the non-circular motions. Alternatively, it could be the result of the superposition of two kinematic components in the gas: the first due to rotation of the gas in the galaxy disc, as for the stars, and the second due to rotation of the gas in the polar ring.

We now investigate the possibility that the SAURON ionized-gas velocity field is indeed due to the superposition of two components, one rotating in the main galaxy (equatorial) plane and the other in the polar ring. Our goal is to check if the features on the SAURON map of the ionized-gas velocity dispersions are consistent with originating from a superposition of gas motions in these two planes. Assuming that we have two gas disks, both characterized by ordered motions, and as the location of high velocities in each of them will be spatially offset, the expectation is that their superposition will effectively be transposed into high velocity dispersion values, offset from the centre, and approximately (but not exactly) along the minor axis of the galaxy.

We used kinemetry to investigate this possibility. The first step was to extract the ordered motions belonging to the gas disc in the equatorial plane. To do this we used the set of best-fitting ellipses from the kinemetric analysis of the stellar velocity field. As the stellar velocity field is very regular, and consistent with axisymmetry (Krajnovic et al. 2011), these ellipses trace circular orbits in the equatorial plane. As Fig. 9 shows the orientation of these ellipses is on average 55° offset from the gas motions, as mentioned above. We show the ellipses overplotted on the gas velocity field in Fig. 10(a). The velocity component that is obtained in this way we

call $V_{\rm rot\_gas}$, and show it in panel (b). Under kinemetry assumptions this component contains the motions of gas clouds in the equatorial plane and on circular orbits.

The gas component that is not within the equatorial plane can be derived by subtraction, $V_{\rm polar} = V_{\rm gas} - V_{\rm rot\_gas}$, and we show it in panel (c). We tentatively call it a 'polar' component, as the velocity field is aligned with the minor axis of the galaxy and the observed polar ring. The next step is to run kinemetry on this $V_{\rm polar}$ field. In Fig. 10(d), we show the ordered motions belonging to this gas component, and call it $V_{\rm rot\_polar}$. This component, under assumptions of the kinemetric analysis, represents the part of the gas that is on circular orbits in the polar disc/ring.

As mentioned above, our goal is to check if the main features of the gas velocity dispersion field can be reproduced by the superposition of motions in the equatorial and polar planes. We do this by looking at the absolute differences between the velocity fields in panels (b) and (d), or the difference between the ordered motions in the two planes. The result is shown in panel (f) and should be compared with the map in panel (e). The two maps are qualitatively similar, showing high and low velocity values at the same locations: nearly along the minor and major axes, respectively. The model velocity dispersion map of panel f) is only good as a simplistic approximation of the observed gas velocity dispersion in the SAURON velocity field of NGC 4111 (Fig. 8), but it highlights its consistency with the presence of two main components in the gas. Therefore, we can conclude that the SAURON gas kinematics is consistent with originating from two components which are located at different planes of the galaxy.

4.3 Nuclear scale – NIFS

Here, we discuss the results from the NIFS data, covering the inner ≈110 pc radius, at a spatial resolution of ≈7 pc.

4.3.1 Stellar and molecular (H_2) gas flux distributions

The NIFS flux distribution in the continuum is shown in the right panel of Fig. 5 integrated within the 2.175–2.200 μm wavelength range, revealing a smooth distribution along the galaxy plane from the south-east (SE) to the north-west (NW) of the nucleus.

The H_2(1–0) S(1) line flux map, shown in the left-hand panel of Fig. 5, presents an elongated structure running from the north-east (NE) to the south-west (SW) resembling an inclined ring perpendicular to the galaxy plane and that seems not to be centred at the galaxy nucleus (shown as a cross in the figure). The diameter of the ring is ≈3 arcsec (210 pc), oriented perpendicular to the galaxy plane with a projected width of ≈0.5 arcsec (37 pc) encircling the nucleus. The H_2 flux distribution – stronger to the NW than to the SE of the nucleus – suggests that the NW portion corresponds to the near side of the ring.

4.3.2 Molecular H_2 gas mass and excitation

In order to investigate the origin of the H_2 emission, we first calculate its temperature. We have looked for other emission lines and found that in some regions of the ring, and in particular at the brightest spot to the SW, at 1.3 arcsec (95 pc) from the nucleus, two other H_2 emission lines could be measured: $H_2\lambda2.0338$ μm and $H_2\lambda2.4066$ μm.

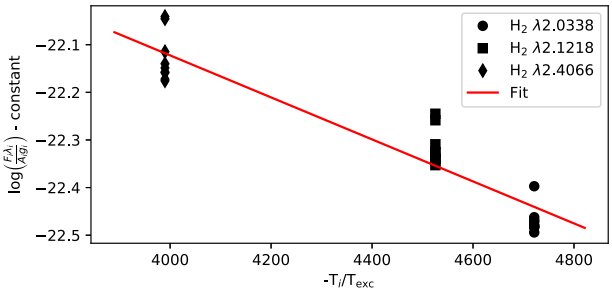

Figure 11. Relation derived using equation (1) from Wilman, Edge & Johnstone (2005). The black dot, square, and diamond show values for the lines H_2 λ2.0338 μm, λ2.1218 μm, and λ2.4066 μm, respectively. The red line is a linear fit to the data, with an angular coefficient $-1/2267$ K^{-1}.

The H_2 gas temperature was obtained using the relation from Wilman et al. (2005) applied to the three emission lines above:

$$\log\left(\frac{F_i\lambda_i}{A_i g_i}\right) = \text{constant} - \frac{T_i}{T_{\rm exc}}, \quad (1)$$

where F_i is the flux from the $i^{\rm th}$ H_2 emission line, λ_i is its wavelength, A_i is the spontaneous emission coefficient, g_i is the statistical weight of the upper level of the transition, and T_i is the level energy expressed as temperature. The expression above is valid for thermal excitation, assuming an *ortho*:*para* abundance ratio of 3:1. From this expression, we obtain $T_{\rm exc} = 2267 \pm 166$ K for the gas as the inverse of the gradient of the linear fit to the data, as shown in Fig. 11, adopting the uncertainty from the correlation matrix of the linear regression. $T_{\rm exc}$ is the kinetic temperature if the H_2 gas is in thermal equilibrium.

We use the flux distribution in the $H_2\lambda2.1218$ μm line to calculate the hot H_2 gas mass according to the expression (Scoville et al. 1982; Riffel et al. 2008):

$$M_{\rm hot\ H_2} = \frac{2m_{\rm p}\ F_{\rm H_2\lambda2.1218}\ 4\pi D^2}{f_{v=1,J=3}\ A_{S(1)}\ h\nu}, \quad (2)$$

where $m_{\rm p}$ is the proton mass, $F_{\rm H_2\lambda2.1218}$ is the line flux, D is the distance to the galaxy, $f_{v=1,J=3}$ is the population fraction and $A_{S(1)}$ is the transition probability. The gas mass is obtained in solar masses. Using $T = 2267 \pm 166$ K (obtained above), the population fraction is $f_{v=1,J=3} = 1.22 \times 10^{-2}$, and the transition probability is $A_{S(1)} = 3.47 \times 10^{-7}$ s^{-1} (Turner, Kirby-Docken & Dalgarno 1977; Scoville et al. 1982; Riffel et al. 2008). Using these parameters, we obtain a mass for the hot molecular gas $M_{\rm hot\ H_2} = 139.48 \pm 4.38$ M$_\odot$.

This mass is very small but is only be the 'hot skin' of the H_2 total mass, which should be dominated by cold gas. A number of studies have compared H_2 masses obtained using the cold CO molecular lines (observed at mm wavelengths) with that of hot H_2 observed in the near-IR for the nuclear regions of active galaxies. For example, Dale et al. (2005) obtained ratios in the range $10^5 \leq M_{\rm cold\ H_2}/M_{\rm hot\ H_2} \leq 10^7$, Müller Sánchez et al. (2006) in the range $10^6 \leq (M_{\rm cold\ H_2}/M_{\rm hot\ H_2}) \leq 5 \times 10^6$, while Mazzalay et al. (2013), compiling more data, covering a wider range of luminosities than the previous studies have derived the following relation:

$$M_{\rm cold\ H_2} \approx 1174 \left(\frac{L_{\rm H_2\lambda2.1218}}{\rm L_\odot}\right), \quad (3)$$

where $L_{\rm H_2\lambda2.1218}$ is the luminosity of this H_2 line and the standard deviation of the scatter about the factor $\beta = 1174$ is ≈35 per cent. Using the above expression, we obtain $M_{\rm cold\ H_2} \approx (1.01 \pm 0.36) \times 10^8$ M$_\odot$, an order of magnitude larger than the lower limit for the cold gas mass we have obtained from the *HST* colour map (Section 4.1).

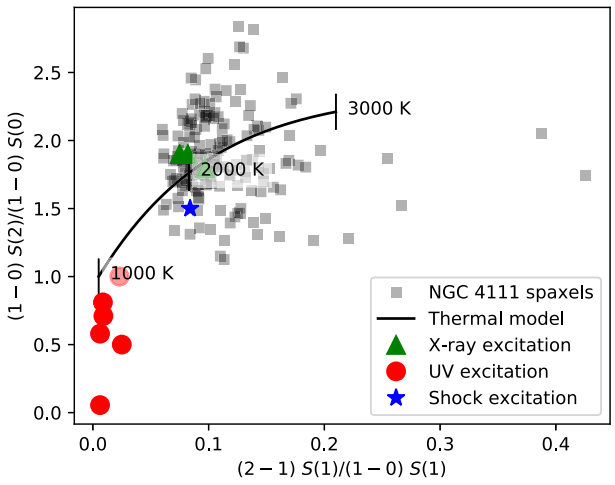

Figure 12. Molecular hydrogen line ratio diagram H_2(1–0)S(2)/H_2(1–0)S(0) *versus* H_2(2–1)S(1)/H_2(1–0)S(1) (Mouri 1994). The grey squares are spaxels from the H_2 ring of NGC 4111. The black curve represents thermal emission models with temperatures in the range of 1000–3000 K. The red circles are the thermal UV excitation models from Sternberg & Dalgarno (1989), the blue star is the shock heating model from Brand et al. (1989), and the green triangles are X-ray heating models by Draine & Woods (1990).

This cold gas mass is comparable to those recently obtained by Schönell et al. (2019), using the same instrument and methodology for a sample of six nearby active galaxies, which are in the range of $8 \times 10^7 M_\odot \leq M_{\rm cold\ H_2} \leq 6 \times 10^8\ M_\odot$.

What physical processes heat the gas to the calculated temperature of ≈2200 K? In order to investigate the nature of the gas excitation, we calculated the H_2(2–1)S(1)/H_2(1–0)S(1) line ratio, as its value can be used to distinguish the excitation mechanism: values of the order of 0.15 ± 0.15 are consistent with thermal processes and values of the order of 0.55 and larger are caused by UV fluorescence (Mouri 1994; Reunanen, Kotilainen & Prieto 2002; Rodríguez-Ardila et al. 2004; Storchi-Bergmann et al. 2009). For NGC 4111, we find a mean value of 0.2 along the H_2 ring, suggesting primarily thermal excitation. The heating mechanism is believed to be the nuclear hard X-ray photons, whose source is apparently embedded in the dusty ring (González-Martín et al. 2009). The lack of fluorescence – that requires the presence of UV photons – is consistent with the absence of the Br γ recombination line in the NIFS spectra, with the UV photons likely being extinguished by the dust surrounding the nucleus and thus not available to ionize the neutral hydrogen. However, the absence of Br γ may also be explained by a lack of stellar formation in the nuclear region – maybe due to heating of the gas by the obscured AGN, despite the existence of available molecular gas in the region.

To further constrain the excitation mechanism, we have used the molecular hydrogen line-ratio diagram from Mouri (1994), shown in Fig. 12, where we have plotted the ratios H_2(1–0)S(2)/H_2(1–0)S(0) *versus* H_2(2–1)S(1)/H_2(1–0)S(1) from the NIFS data as grey squares for the spaxels presenting these lines. This diagram compares line ratios that only take place in *ortho* H_2 molecules [the (2–1)S(1) λ2.2477 μm and (1–0)S(1) λ2.1218 μm transitions] with those in *para* H_2 molecules [the (1–0)S(2) λ2.0338 μm and (1–0)S(0) λ2.2235 μm transitions]. We included only SNR > 2 spaxels in the plot to reduce the scattering caused by noisy spaxels. In the figure, we also include a sequence of the thermal models for temperatures ranging from 1000 K to 3000 K as a black curve. In addition, we include predictions by models according to other possible excitation mechanisms: (1) UV excitation due to fluorescence, shown as red circles (Sternberg & Dalgarno 1989); (2) shock excitation due to outflowing material, e.g. from supernova remnants and/or gas winds, shown as a blue star (Brand et al. 1989); (3) X-ray heating from AGN, shown as green triangles (Draine & Woods 1990). The model data used in Fig. 12 follows Mouri (1994).

The comparison between our data and the models clearly indicates thermal excitation of H_2 with temperatures of about 2000 K and higher (but lower than 3000 K), including heating by X-rays and/or shocks.

4.3.3 *Stellar kinematics in the inner 110 pc*

The top panels of Fig. 13 show maps of the stellar kinematics, with errors obtained using a Monte Carlo technique, with the corresponding maps shown in Fig. B1 of the Appendix. These errors decrease outwards, with mean error values for the centroid velocity, velocity dispersion, Gauss–Hermite moments h_3 and h_4 of 4.9 km s^{-1}, 6.8 km s^{-1}, 0.03, and 0.06, respectively.

The stellar kinematics of Fig. 13 reveal a rotation pattern with blueshifts to the NW and redshifts to the SE. A comparison of the top left-hand panel of Fig. 13 with the top right-hand panel of Fig. 8 shows that the NIFS stellar velocity field within the inner 110 pc is similar to that of the SAURON kinematics at larger scales. The σ map shows a partial ring with radius of about 1 arcsec (73.1 pc) with velocity dispersion values in the range of 140–150 km s^{-1} surrounding a small drop to about 120 km s^{-1} within the inner 0.5 arcsec (∼37 pc), similar to the drop seen in the SAURON data at larger scales. This indicates the presence of a dynamically cold structure, such as a disc. Although its origin is not clear, similar structures have been associated with young to intermediate age stellar population that retains the colder kinematics of the gas from which it has formed and did not reach equilibrium with the bulge velocity field of the older stars yet (Riffel et al. 2010, 2011). This would be consistent with a possible scenario in which gas from the polar ring has been captured and is forming new stars in the centre of the galaxy.

The h_3-map shows small positive values in the blueshifted side of the velocity field, and, similarly negative values in the redshifted side, indicating that the velocity distribution is slightly asymmetric, showing a 'red tail' and a 'blue tail' in the blueshifted and redshifted sides, respectively. The h_4-map shows small negative values (broader than a Gaussian) associated with higher velocity dispersion spaxels and positive h_4 values (narrower than a Gaussian), for the spaxels with lower velocity dispersion. From Monte Carlo simulations, we obtain a mean uncertainty for the velocity, velocity dispersion, h_3 and h_4 maps of 4.9 km s^{-1}, 6.8 km s^{-1}, 0.03, and 0.06, respectively.

The measurements of the stellar velocity, velocity dispersion and the higher Gauss–Hermite moments from the NIFS data – see the $\sigma_{\star_{\rm NIFS}}$ map in the second panel on the upper row of Fig. 13 – will be used in a future work in order to obtain a dynamical model and constrain the SMBH mass $M_\bullet$ (together with those of other targets of our project).

4.3.4 *Molecular gas kinematics*

The maps of the H_2 gas kinematic parameters obtained from the IFSCube fits are shown in the bottom panels of Fig. 13, while the corresponding Monte Carlo error maps are shown in Fig. B1 of the

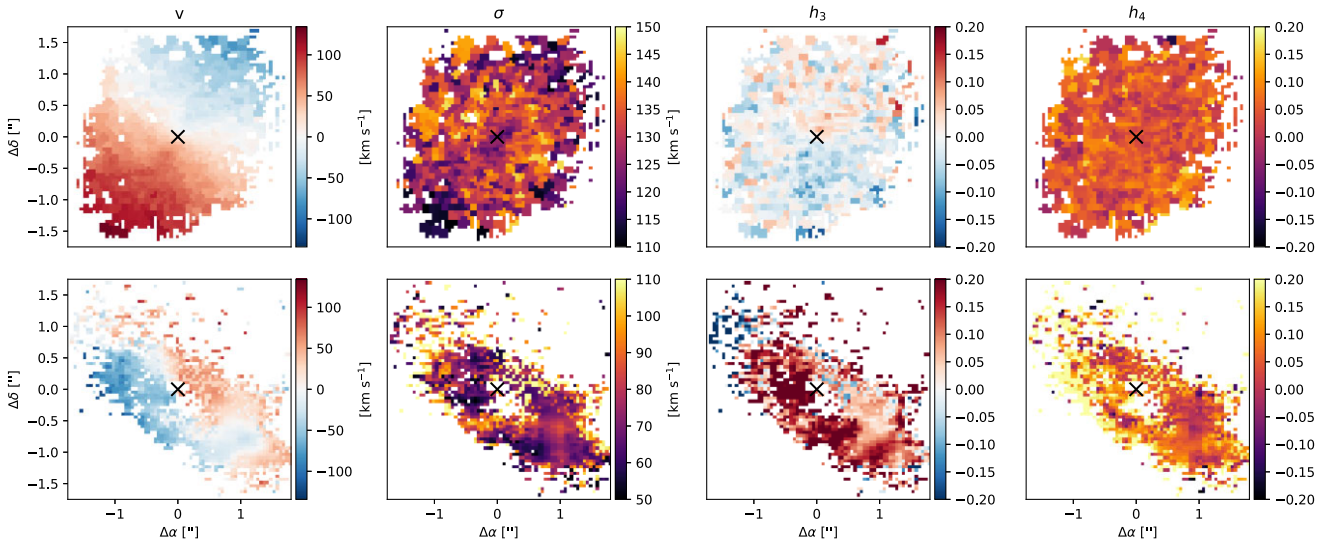

Figure 13. Top: NIFS stellar kinematic maps, from left to right: centroid velocity, velocity dispersion, Gauss–Hermite moments h_3 and h_4. The respective mean Monte Carlo errors are 4.9 km s^{-1}, 6.8 km s^{-1}, 0.03, and 0.06. Bottom: As in the top panels, for the molecular gas kinematics (H_2 λ2.1218 μm), with mean errors of 17.9 km s^{-1}, 39.5 km s^{-1}, 0.05, and 0.04, respectively. For error maps see Fig. B1 of the Appendix. The cross indicates the location of the galaxy nucleus.

Appendix. The mean errors in the parameters v, σ, h_3, and h_4, are, respectively, 17.9 km s^{-1}, 39.5 km s^{-1}, 0.05, and 0.04.

The H_2 velocity field shows redshifts to the NW and blueshifts to the SE, thus opposite to the observed velocities of the stellar velocity field. This kinematics is also distinct from the [O III] kinematics that present blueshifts to the S-SW and redshifts to the N-NE. Nevertheless, we point out that the [O III] emission line probes the ionized gas kinematics on kpc scales and the H_2 emission probes the molecular gas kinematics at 10–100 pc scales. The velocity dispersion is roughly ∼70 km s^{-1} all along the H_2 ring, with some higher values from the NW to the NE part of the ring. The h_3-map shows the same kind of correlation with the velocity field as shown by the stellar kinematics maps: positive h_3 values in the blueshifted side of the ring – a 'red tail' on the profiles – and negative values for the redshifted side of the ring – a 'blue tail' on the profiles. The positive h_3 values are nevertheless much higher than the negative values, indicating the presence of red wings in most regions of the ring. The h_4 values are predominantly positive, presenting a similar relation to that observed for the stellar velocity field, where negative values are in general associated with higher velocity dispersion and positive values with lower velocity dispersion. From Monte Carlo simulations, we obtain a mean uncertainty for the velocity, velocity dispersion, h_3 and h_4 maps of 17.9 km s^{-1}, 39.5 km s^{-1}, 0.05, and 0.04, respectively, which are quite higher than the uncertainties in the stellar kinematics. We present the Monte Carlo error maps for the NIFS stellar and molecular gas kinematics in Fig. B1 of the Appendix.

As pointed out above, the H_2 gas kinematics (the bottom panels of Fig. 13) suggest counter rotation of the molecular ring relative to the stellar kinematics – but the kinemetry analysis of Section 4.3.6 reveal an angle between the stellar and gas apparent rotation varying in the range of 120°–160°, thus smaller than 180°, suggesting another interpretation. As the apparent near side of the ring – that we hypothesize is the NW because it is brighter than the SE – shows redshifts and the back (far) side shows blueshifts, an alternative interpretation is that the ring of molecular gas could be falling towards the galaxy centre.

4.3.5 *H_2 channel maps*

The higher order moment maps of Fig. 13 indicate some complexity in the H_2 kinematics that is better illustrated via the channel maps shown in Fig. 14, obtained with IFSCube.

In these maps, the H_2(1–0) S(1) line profiles have been sliced in velocity bins centred on velocities ranging from –165 to 165 km s^{-1} with a 30 km s^{-1} channel width. They show that the fastest blueshifts are observed in three compact regions: the smallest is just ≈0.2 arcsec (15 pc) to the SE of the nucleus, the second is 0.5 arcsec south of the nucleus and the last at 1.3 arcsec (95 pc) to the SW, corresponding to the brightest spot of the molecular ring (seen in the left-hand panel of Fig. 5 marked with a blue *B*). In the −135 to −75 km s^{-1} velocity range, the three aforementioned regions gradually enlarge and begin to reveal the SE half of the annular structure. The bright-spot 1 arcsec SW of the nucleus seems to keep its flux up to −15 km s^{-1}. The −75 to 45 km s^{-1} channels show that the flux gradually increases to the NW of the nucleus and fades from the SE, with only emission in a knot to the south and emission to the SW of the nucleus still being detected. In the 75 to 165 km s^{-1} range, the flux in each channel gradually diminishes, increasing again at 135 km s^{-1}. The fastest redshifted component at 165 km s^{-1} is located within ≈0.5 arcsec (36 pc) of the nucleus, towards the NW, opposite to the fastest blueshifted region just to the SE of the nucleus. We interpret this change in orientation as follows: if the NW is indeed the near side of the ring, this velocity pattern does indicate infall towards the centre of the galaxy. We do not see indication of rotation along the ring, as, if this were the case, we should observe the highest velocities at the SW and NE tips of the ring that should also be opposite to each other. We do not see this; the highest velocities are observed to the SE and NW. The channel maps further show that the highest velocity regions tend to be closer to the nucleus than the lower velocity regions, suggesting an inwards acceleration, also consistent with an inflow scenario.

To further evidence the signature of inflow, we calculated the average projected radial distance ⟨r⟩ of the H_2 gas for each kinematic channel. We present the channel velocity values as a function of these radii in Fig. 15. As expected, the mean radial distances decrease as

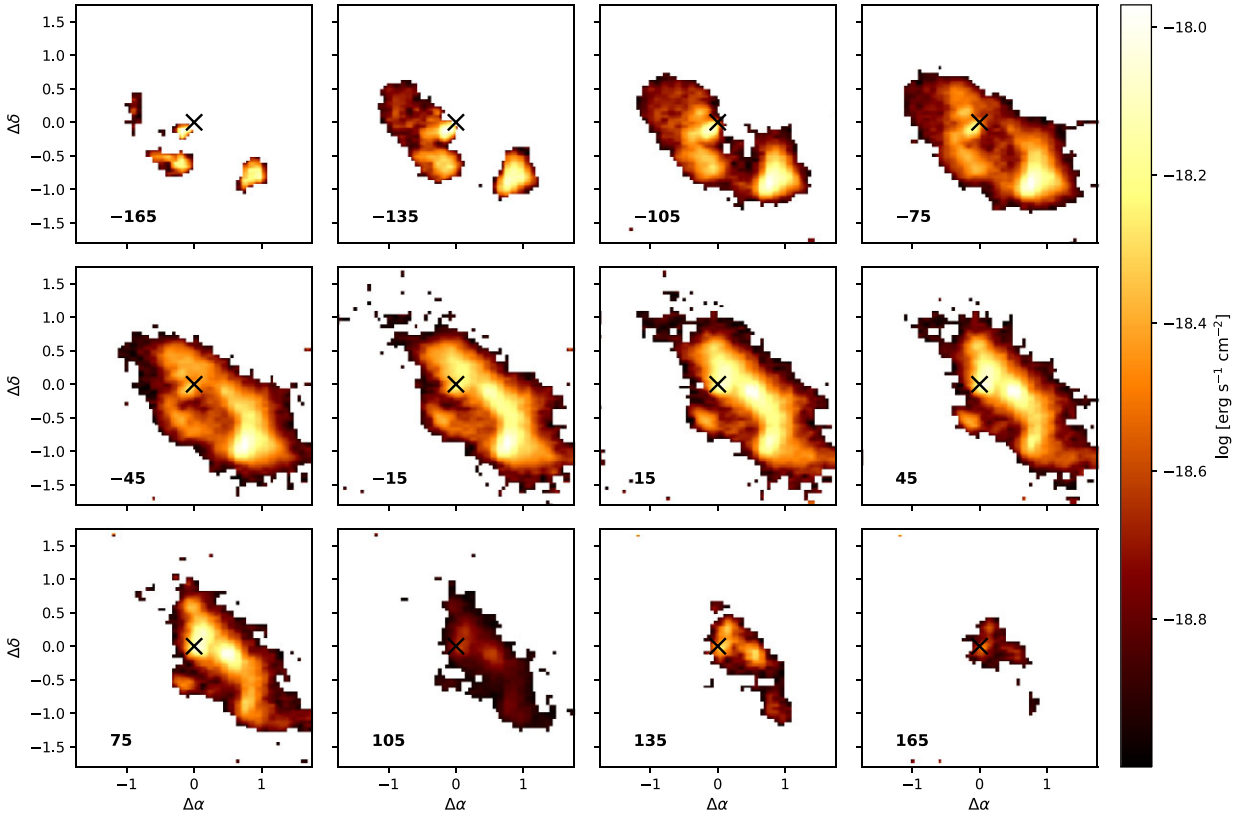

Figure 14. Channel maps of the $H_2\lambda2.1218$ μm emission line, centred at the velocities listed in the bottom left of each panel in units km s^{-1}. The cross indicates the location of the galaxy nucleus.

the velocities increase, supporting acceleration of the molecular gas towards the nucleus in an inflow.

4.3.6 *Kinemetric analysis*

We have also applied kinemetry to investigate the NIFS stellar and molecular gas kinematics, as we have done to investigate the SAURON kinematics.

The results from the kinemetry analysis for the stellar and H_2 gas velocity fields from the NIFS data – major axis *PA* and rotation velocities V_{rot} are shown, together with those for the SAURON data in the two panels of Fig. 9.

The NIFS stellar velocities rise more steeply than the SAURON velocities (as expected given the sharper PSF of NIFS), but otherwise are fully consistent. One other observation is worth remarking: while H_2 and stellar velocities from the NIFS data have similarly steep rise and amplitudes, molecular gas being marginally faster (expected, e.g. Young, Bureau & Cappellari 2008), the ionized gas in the SAURON data is significantly slower in the central region. This is a clear indication that its clouds are neither in a thin disk configuration nor are on circular orbits.

The top panel of Fig. 9 shows that the H_2 kinemetry reveals a misalignment between the H_2 and stellar kinematics of ≈155°, indicating that, besides the ionized gas on large scales being misaligned relative to the stellar kinematics, the gas in the central region is also in an unstable configuration and that gas clouds are not moving on purely circular orbits. We show this in the three panels of Fig. 16. The first panel shows the same H_2 velocity field of Fig. 13, which

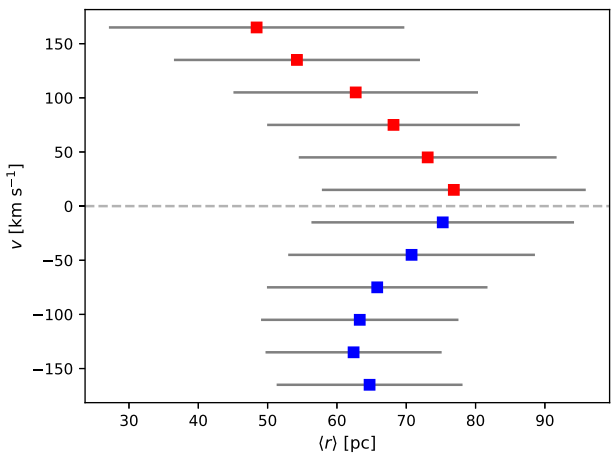

Figure 15. Average projected radial distance ⟨*r*⟩ for each kinematic channel of the H_2 emitting gas from Fig. 14, including the RMS variation of the distances in each channel as a grey bar. In red (blue), we indicate the redshifted (blueshifted) channels.

is followed by the kinemetric reconstruction of a 'circular' velocity map, V_{disc}. This map is reconstructed using the V_{rot} of the molecular gas (as shown in Fig. 9), but assuming that the orientation of the field is constant: we fixed it to the median value of 305° (the top panel of Fig. 9). As the H_2 gas shows some variation in the PA and large values of the other harmonic coefficients, $V_{disc} \neq V_{circ}$. Nevertheless,

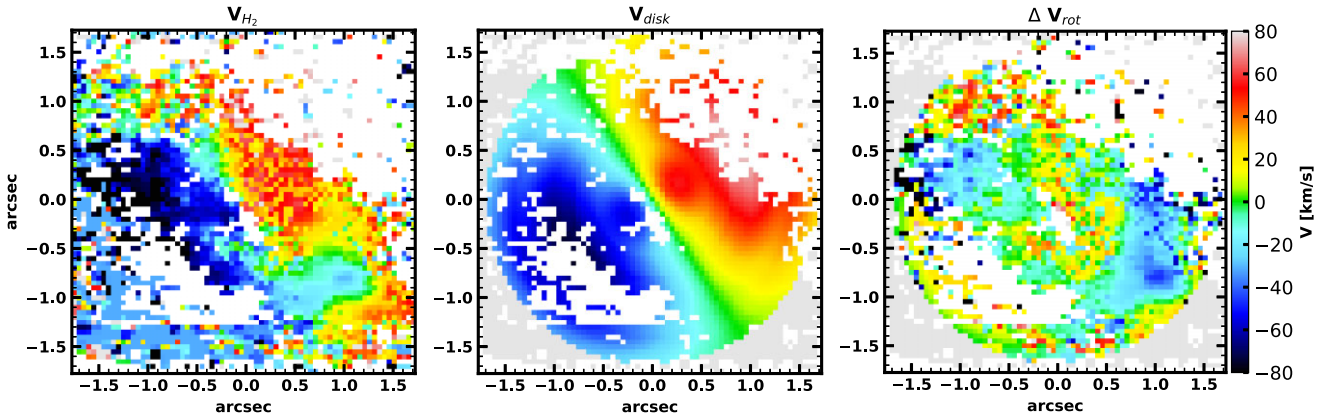

Figure 16. NIFS H_2 kinematics (left), its kinemetry fitting (centre) and the residual between the two (right), showing evidence of non-circular components in the velocity field.

it can be used as first-order approximation to gauge the contribution of non-circular motions in the molecular gas kinematics, shown on the residuals in the last panel of Fig. 16.

5 SCENARIO

In this section, we use the results from the large-scale gas distribution (*HST*), excitation and kinematics (SAURON) as compared to those of the nuclear scale (NIFS) to propose a scenario for the physical processes occurring within the inner kpcs of NGC 4111.

5.1 Comparison between the large and nuclear scale kinematics

The stellar velocity maps of the large-scale SAURON and nuclear scale NIFS data – characterized via kinemetry in Fig. 9 – are remarkably similar: they share the same position angle and flattening (not shown), and have minimal residuals in higher order harmonic coefficients (also not shown).

Nevertheless, the large-scale [O III] gas kinematics and the nuclear-scale H_2 kinematics look distinct, but a closer look reveals that they seem to be physically connected. This connection between the large-scale ionized gas and the nuclear-scale molecular gas is suggestively shown in Figs 17 and 18.

Fig. 17 shows a comparison between the residuals of the [O III] and H_2 velocity fields relative to the stellar velocity field. Inspection of the [O III] residuals within the NIFS FoV suggest blueshifts to the SE and redshifts to the NW, as observed in the H_2 residuals, suggesting that the large-scale ionized gas kinematics connect with the nuclear scale H_2 gas kinematics.

We now consider the hypothesis discussed in Section 4.2.4 in which the SAURON ionized-gas velocity field is due to the superposition of two kinematic components, one rotating in the main galaxy (equatorial) plane and the other in the polar ring. In the top panel of Fig. 18, we have used the results from the kinemetry of the polar ring (Fig. 16) to obtain residuals between the observed velocities and its reconstructed circular velocity field. The residuals suggest the presence of a pattern in the shape of spiral arms, outlined by the black lines in the figure. This spiral configuration is suggestive of inflows, as observed in previous kinematic studies (e.g. Storchi-Bergmann & Schnorr-Müller 2019, and references therein). The small square in the top panel shows the NIFS FoV, with the NIFS H_2 velocity field shown in the bottom panel. Although the angular resolution of the SAURON data is much lower that of the NIFS data, a careful inspection of the residual velocity field of the top panel shows that, within the NIFS FoV (black square) there is a hint of residual redshifts towards the NW and residual blueshifts to the SE, suggesting again a connection between the large-scale ionized gas velocity field and the nuclear scale H_2 velocity field, which also shows redshifts to the NW and blueshifts to the SE.

The above results, in which the large scale [O III] gas kinematics seems to connect with the nuclear scale H_2 gas kinematics implies that, if we can conclude that the H_2 kinematics indicates inflow, this inflow seems to be present also in the larger scale gas, or at least originate in the large-scale gas.

5.1.1 The scenario

We propose the following scenario to explain the observations from the inner ≈1.5 kpc radius probed by the *HST* and SAURON data down to the inner ≈110–10 pc radii probed by the NIFS data. The dusty polar ring probably originates from the capture of a dwarf galaxy by NGC 4111, consistent with the estimated lower limit of the gas mass of $\approx 10^7$ $M_\odot$ obtained from the extinction map of the 450 pc ring. The ionized gas seen in the SAURON data is present in both the galaxy disc and the polar ring structures. The increase in its velocity dispersion in the region of the polar ring can be attributed to the superposition of two kinematic components: rotation in the galaxy plane and orbital motion in the polar ring. This orbital motion shows a disturbed rotation pattern, revealed by the kinemetry analysis, such that the residual motion relative to the rotation suggests the presence of a spiral-like structure that seems to connect with the H_2 kinematics within the inner ≈110 pc, as suggested by the two panels of Fig. 17.

The residual inspiral in NGC 4111, seen in Fig. 18, resembles nuclear spirals (on 100 pc scales) associated to inwards motion of gas found in previous studies of the AGNIFS (AGN Integral Field Spectroscopy) group, such as those in the nearby active galaxies NGC 7213 (Schnorr-Müller et al. 2014), NGC 1667 (Schnorr-Müller et al. 2017) and NGC 2110 (Diniz et al. 2019), and also the nuclear spirals found in NGC 1097 (Davies et al. 2009; van de Ven & Fathi 2010; Fathi et al. 2013). Other observational (e.g. Combes et al. 2014) and theoretical (Kim & Elmegreen 2017) studies also support the presence of inflows along nuclear spirals in nearby active galaxies.

The H_2 ring kinematics – that seems to connect with the above spirals, suggests inward motion: assuming that the brighter NW side is the near and the fainter SE side is the far, the blueshifts observed in

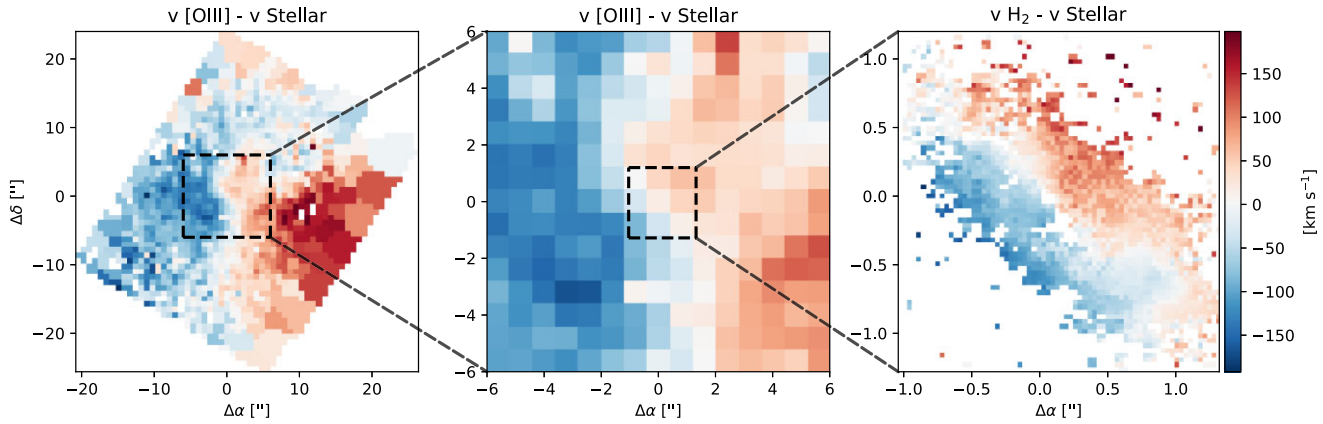

Figure 17. Comparison between the kpc-scale (SAURON) v[O III] and the 100 pc scale (NIFS) H_2 gas velocity fields after the subtraction of the stellar velocity field. In the left-hand panel, the dashed square shows the FoV from the central panel; in the central panel, the dashed square shows the NIFS FoV over the zoomed-in velocity field of the left-hand panel.

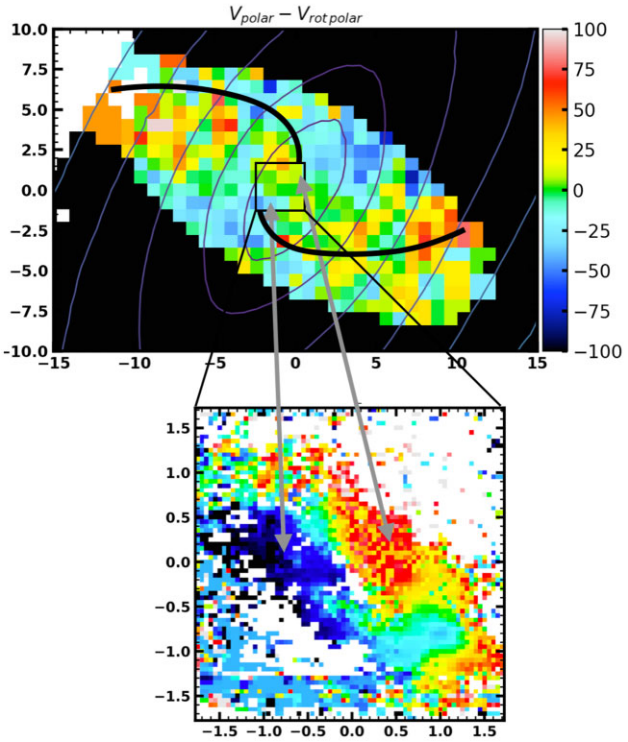

Figure 18. Top: Residual map between the ionized gas polar ring velocities and its reconstructed circular velocity field from kinemetry, with the black lines delineating an apparent spiral structure. The small square shows the 3 arcsec × 3 arcsec NIFS FoV. Bottom: the NIFS H_2 velocity field showing redshifts to the NW and blueshifts to the SE that apparently connect with the residuals of the SAURON gas kinematics.

the far side and redshifts observed in the near side indicate inflows. The channel maps of Fig. 14 and the fact that the average radius of the channel maps decrease as the velocity increases, support such inflows, suggesting, in addition, inwards acceleration.

The inflowing gas may be settling in the galaxy plane and forming new stars there, and could be the cause of the observed sigma drop in the NIFS and SAURON data stellar kinematics. Both σ-drop structures could be part of the same gas-rich merger event, building the large-scale and small-scale discs and gas structures as the merger evolves. At least part of the inflowing gas seems to be reaching the nucleus, triggering a low-luminosity AGN that can be observed in X-rays. This emission – possibly combined with shocks in the region – is the source of excitation of the H_2, as discussed in Section 4.3.2.

Having concluded that the observed gas kinematics indicate inflows towards the nucleus, we have used the NIFS data to estimate the mass inflow rate and compare it to the mass accretion rate to the obscured AGN. For this, we need first to obtain an estimate for the SMBH mass as well as the AGN accretion rate and Eddington ratio.

5.2 SMBH mass and Eddington ratio

We use the integrated $\sigma_\star$ value within one effective radius $\sigma_{\star\mathrm{SAURON}} = 163.3 \pm 8.1$ km s^{-1}, as previously determined from the SAURON data by Cappellari et al. (2013) in order to estimate $M_\bullet$ with the empirical $M_\bullet - \sigma_\star$ relation from van den Bosch (2016):

$$\log\left(\frac{M_\bullet}{\mathrm{M}_\odot}\right) = (8.32 \pm 0.04) + (5.35 \pm 0.23)\log\left(\frac{\sigma_\star}{200\ \mathrm{km\ s^{-1}}}\right). \quad (4)$$

For $\sigma_\star = \sigma_{\star\mathrm{SAURON}}$, we obtain $M_\bullet = (7.06^{+2.62}_{-1.79}) \times 10^7\ \mathrm{M}_\odot$. This value is consistent with a previous estimate by Nyland et al. (2016) of $M_\bullet = 6.31 \times 10^7\ \mathrm{M}_\odot$, obtained with the $M_\bullet - \sigma_\star$ relation from McConnell & Ma (2013).

The bolometric luminosity L_{bol} was obtained from the X-ray luminosity in the 0.5–10.0 keV range (González-Martín et al. 2009), assuming that this luminosity represents 8 per cent of the total luminosity of the AGN (Nemmen et al. 2006). This allows us to calculate the Eddington ratio $L_{\mathrm{bol}}/L_{\mathrm{Edd}} = 1.5^{+0.5}_{-0.4} \times 10^{-4}$ for NGC 4111, using our determined value of the SMBH mass above. The low Eddington ratio suggests that, if there is an active nucleus in NGC 4111, as indicated from the emitted X-rays, the accretion regime is that of a radiatively inefficient accretion flow (RIAF).

5.3 Mass inflow rate and the mass accretion rate

We have estimated the mass inflow rate $\dot{m}_{\mathrm{inf}}$ using the channel maps from Fig. 14 and the following expression:

$$\dot{m}_{\mathrm{inf}} = \frac{mv}{\langle r \rangle}, \quad (5)$$

where $\langle r \rangle$ is the average radial distance of H_2 in each channel (Fig. 15), v is the channel velocity, and m is the integrated gas mass from each channel, determined using equation (2) for the hot molecular gas and equation (3) for the cold.

One important question is: What fraction of the gas is actually inflowing? In our previous studies cited above, as well as suggested in Figs 16 and 18, the residuals from rotation orbital velocity are usually observed in spiral structures covering ≈10 per cent of the observed velocity field. We have then tentatively considered this fraction of the gas in each channel that is actually inflowing.

We first considered only the hot phase of the gas in this calculation and obtain a mass inflow rate of only $7.8^{+3.4}_{-1.7} \times 10^{-4}$ $M_\odot$ yr^{-1}. Nevertheless, as discussed above, the hot phase of the gas is probably only 'the heated skin' of a much larger gas reservoir, dominated by the cold gas.

Considering now the cold component and that gas from all channels is inflowing, we determine an upper limit for the mass inflow rate of $56.9^{+24.1}_{-12.5}$ $M_\odot$ yr^{-1}.

We then considered that only the two highest velocity channels (−165, −135, 135, and 165 km s^{-1}) trace the inflows, with the lower velocity gas tracing gas orbiting in the galaxy plane. The resulting mass inflow rate is $33.9^{+16.3}_{-7.9}$ $M_\odot$ yr^{-1}.

In order to obtain still another estimate, instead of using equation (3) to estimate the mass of cold gas, we used the value of hot molecular gas obtained with equation (2) and the lower limit of the ratio between the cold and hot molecular gas masses from Dale et al. (2005) of 10^5. This way we obtain a lower limit of $7.9^{+3.3}_{-1.7}$ $M_\odot$ yr^{-1} for the mass inflow rate.

The mass accretion rate $\dot{m}_{\rm acc}$ was determined using the expression:

$$\dot{m}_{\rm acc} = \frac{L_{\rm bol}}{\eta c^2} \quad (6)$$

using the previously calculated $L_{\rm bol}$ and assuming an accretion efficiency $\eta = 0.01$, justified by the low Eddington ratio for this AGN (Nemmen et al. 2006), the resulting mass accretion rate is 0.002 $M_\odot$ yr^{-1}, which supports the presence of an RIAF in the nucleus of NGC 4111.

The above accretion rate is larger than the mass inflow rate in hot molecular gas, but is much lower than the estimated mass inflow rate in cold molecular gas, that should dominate the mass of molecular gas, as previously pointed out. This indicates that cold molecular gas could be accumulating in the nuclear region and is enough to trigger new episodes of star formation and stronger nuclear activity in the near future. At a mass-inflow rate of ≈5–10 $M_\odot$ yr^{-1}, the existing cold gas reservoir of $\approx 10^8 M_\odot$ should keep this process going for the next 10^7 yr.

6 CONCLUSIONS

We have analysed galactic scale *HST* images of the nearby S0 polar-ring galaxy NGC 4111 through the F475W and F160W filters together with SAURON optical IFS of the inner 1.5 kpc radius and nuclear scale K-band Gemini NIFS AO-assisted IFS of the inner 110 pc radius. Our main conclusions are as follows:

(i) The *HST* images reveal the dusty polar ring extending by ∼450 pc perpendicular to the plane of the galaxy. From the colour map F475W-F160W, we obtain an extinction map and a lower limit for the cold gas mass in the ring as $M_{\rm gas} = 9.8 \times 10^6$ $M_\odot$. This mass is consistent with an origin from a captured dwarf galaxy.

(ii) Ionized gas emission is seen in the SAURON data, with line ratio values $1 \leq$ [O III]λ4959, 5007 Å/H $\beta \leq 3$ supporting the LINER classification of previous studies.

(iii) The NIFS data show a hot molecular gas ring with diameter of 220 pc – embedded in the dusty polar ring above – with a calculated temperature of 2267 ± 166 K and mass $M_{\rm hot\,H_2} = 139.5 \pm 4.4 M_\odot$. This hot gas mass corresponds to an estimated cold gas mass of $M_{\rm cold\,H_2} \approx 10^8$ $M_\odot$ within the inner 110 pc (radius) which is consistent with the lower limit for the gas mass obtained from the *HST* images and further suggests an extragalactic origin for this gas.

(iv) The excitation of the hot H_2 is thermal, most probably due to X-ray heating, supporting the presence of an AGN at the nucleus. Although shocks could also contribute to the gas excitation, the low velocity dispersion (∼60 km s^{-1}) does not support a major contribution of shocks to the H_2 excitation.

(v) The large scale (1.5 kpc radius) SAURON and smaller scale (110 pc radius) NIFS stellar velocity distributions show the same rotation pattern, as supported also by kinemetry analysis.

(vi) Both the large- and small-scale stellar velocity dispersion $\sigma_\star$ show drops in their values along the galaxy major axis, within radii of ≈350 and ≈35 pc, respectively. This is probably associated with recent capture of gas (on both scales) that settled in a disc and formed new stars that have still kept their colder gas kinematics as compared to the surrounding bulge. The presence of younger stars in the region is supported by previous studies of the stellar population.

(vii) Both the 1.5 kpc scale [O III] and the 110 pc scale hot H_2 velocity fields are distinct from the stellar one, indicating that the gas in both ionized and molecular phases is not in a stable configuration.

(viii) The [O III] gas kinematics show two components: (1) rotation similar to that of the stars in the galaxy plane; (2) disturbed rotation along the dusty polar ring. Velocity residuals relative to the rotation component in the ring show an spiral pattern suggestive of inflows that seem to connect to the H_2 velocity field in the 110 pc ring.

(ix) The H_2 velocity field in the 110 pc ring shows blueshifts in the apparent far side and redshifts in the apparent near side, as well increasing velocity towards the inner regions in channel maps, indicating inflows towards the nucleus.

(x) We have estimated the mass inflow rate towards the nucleus from the H_2 channel maps and the expected corresponding cold molecular gas mass, finding values of 5–10 $M_\odot$ yr^{-1}. Such values are much larger than the accretion rate to the AGN and enough to feed new episodes of star formation within the inner few pc to100 pc, considering the available gas reservoir of ≈ 10^8 $M_\odot$.

We conclude that our data supports a scenario in which a dwarf, gas-rich galaxy has been recently captured by NGC 4111 giving origin to its polar ring. Part of this gas is flowing in and possibly forming new stars while another part of it seems also to have just reached the nuclear SMBH triggering a so-far low-luminosity AGN. This AGN is already emitting X-rays that are heating the gas and causing thermal excitation of the H_2 molecule. However, as we do not see Br γ in our *K*-band data, UV photons are not reaching the observed gas, which suggests that either new stars have not begun to form and/or these stars and the AGNs are still buried in the dust rich environment, supporting that the AGN has only recently been triggered.

ACKNOWLEDGEMENTS

We thank the anonymous referee that helped us in improving our paper.

This research is based on observations obtained at the international Gemini Observatory, a programme of NSF's NOIRLab, which is managed by the Association of Universities for Research in Astronomy (AURA) under a cooperative agreement with the National Science Foundation, on behalf of the Gemini Observatory partnership: the National Science Foundation (United States), National

Research Council (Canada), Agencia Nacional de Investigación y Desarrollo (Chile), Ministerio de Ciencia, Tecnología e Innovación (Argentina), Ministério da Ciência, Tecnologia, Inovações e Comunicações (Brazil), and Korea Astronomy and Space Science Institute (Republic of Korea).

This research is based on observations made with the NASA/ESA *Hubble Space Telescope* obtained from the Space Telescope Science Institute, which is operated by the Association of Universities for Research in Astronomy, Inc., under NASA contract NAS 5-26555. These observations are associated with programme GO-15323.

Research of Texas A&M has been supported by NSF grant no. AST-1814799.

GvdV acknowledges funding from the European Research Council (ERC) under the European Union's Horizon 2020 research and innovation programme under grant agreement no. 724857 (Consolidator Grant ArcheoDyn).

DATA AVAILABILITY

The *HST* data used in this work is publicly available at https://archive.stsci.edu/hst/ with project code 15323. The GEMINI data are available online via the GEMINI archive at https://archive.gemini.edu/searchform/, with project code GN-2019A-LP-8. Finally, the SAURON data are available via the Isaac Newton Group archive at http://casu.ast.cam.ac.uk/casuadc/ingarch/query identified with observation run numbers 958460, 958461, 958462, 958463, 958464, 958465, and 958466. The maps produced from these data can be shared on reasonable request to the corresponding author.

REFERENCES

Bacon R. et al., 2001, MNRAS, 326, 23
Baldwin J. A., Phillips M. M., Terlevich R., 1981, Publ. Astron. Soc. Pac., 93, 5
Barth A. J., Ho L. C., Filippenko A. V., Sargent W. L. W., 1998, ApJ, 496, 133
Boccas M. et al., 2006, Society of Photo-Optical Instrumentation Engineers (SPIE) Conference Series, 6272, 662723L
Brand P. W. J. L., Toner M. P., Geballe T. R., Webster A. S., Williams P. M., Burton M. G., 1989, MNRAS, 236, 929
Cappellari M. et al., 2011, MNRAS, 413, 813
Cappellari M. et al., 2013, MNRAS, 432, 1709
Cappellari M., Copin Y., 2003, MNRAS, 342, 345
Cappellari M., Emsellem E., 2004, Publ. Astron. Soc. Pac., 116, 138
Cid Fernandes R., Stasinska G., Schlickmann M. S., Mateus A., Vale Asari N., Schoenell W., Sodré L., 2010, MNRAS, 403, 1036
Combes F. et al., 2014, A&A, 565, A97
Dale D. A., Sheth K., Helou G., Regan M. W., Hüttemeister S., 2005, AJ, 129, 2197
Davies R. I., Maciejewski W., Hicks E. K. S., Tacconi L. J., Genzel R., Engel H., 2009, ApJ, 702, 114
Diniz M. R., Riffel R. A., Storchi-Bergmann T., Riffel R., 2019, MNRAS, 487, 3958
Draine B. T., Woods D. T., 1990, ApJ, 363, 464
Emsellem E. et al., 2004, MNRAS, 352, 721
Falcón-Barroso J., Sánchez-Blázquez P., Vazdekis A., Ricciardelli E., Cardiel N., Cenarro A. J., Gorgas J., Peletier R. F., 2011, A&A, 532, A95
Fathi K. et al., 2013, ApJ, 770, L27
Gonzaga S., Hack W., Fruchter A., Mack J., 2012, The DrizzlePac Handbook, Space Telescope Science Institute, *HST* Data Handbook
González-Martín O., Masegosa J., Márquez I., Guainazzi M., Jiménez-Bailón E., 2009, A&A, 506, 1107
Herriot G. et al., 2000, Adaptive Optical Systems Technology, 4007, 115
Ho L. C., Filippenko A. V., Sargent W. L., 1995, ApJS, 98, 477
Ho L. C., Filippenko A. V., Sargent W. L. W., 1997, ApJ, 487, 568
Karachentsev I. D., Nasonova O. G., Courtois H. M., 2013, MNRAS, 429, 2264
Kasparova A. V., Katkov I. Y., Chilingarian I. V., Silchenko O. K., Moiseev A. V., Borisov S. B., 2016, MNRAS, 460, L89
Kauffmann G. et al., 2003, MNRAS, 346, 1055
Kewley L. J., Dopita M. A., Sutherland R. S., Heisler C. A., Trevena J., 2001, ApJ, 556, 121
Kim W.-T., Elmegreen B. G., 2017, ApJ, 841, L4
Krajnovic D. et al., 2008, MNRAS, 390, 93
Krajnovic D. et al., 2011, MNRAS, 414, 2923
Krajnovic D., Cappellari M., de Zeeuw P. T., Copin Y., 2006, MNRAS, 366, 787
Mazzalay X. et al., 2013, MNRAS, 428, 2389
McConnell N. J., Ma C.-P., 2013, ApJ, 764, 184
McDermid R. M. et al., 2015, MNRAS, 448, 3484
McGregor P. J. et al., 2003, 4841, 1581
Mouri H., 1994, ApJ, 427, 777
Müller Sánchez F., Davies R. I., Eisenhauer F., Tacconi L. J., Genzel R., Sternberg A., 2006, A&A, 454, 481
Neistein E., Netzer H., 2014, MNRAS, 437, 3373
Nemmen R. S., Storchi-Bergmann T., Yuan F., Eracleous M., Terashima Y., Wilson A. S., 2006, ApJ, 643, 652
Nyland K. et al., 2016, MNRAS, 458, 2221
Pak M., Rey S.-C., Lisker T., Lee Y., Kim S., Sung E.-C., Jerjen H., Chung J., 2014, MNRAS, 445, 630
Reunanen J., Kotilainen J. K., Prieto M. A., 2002, MNRAS, 331, 154
Riffel R. A., Storchi-Bergmann T., Winge C., McGregor P. J., Beck T., Schmitt H., 2008, MNRAS, 385, 1129
Riffel R. A., Storchi-Bergmann T., Riffel R., Pastoriza M. G., 2010, ApJ, 713, 469
Riffel R., Riffel R. A., Ferrari F., Storchi-Bergmann T., 2011, MNRAS, 416, 493
Rodríguez-Ardila A., Pastoriza M. G., Viegas S., Sigut T. A. A., Pradhan A. K., 2004, A&A, 425, 457
Ruschel-Dutra D., Oliveira B. D. D., 2020, danielrd6/ifscube v1.0
Sarzi M. et al., 2017, Astrophysics Source Code Library, record ascl:1708.012
Savage B. D., Mathis J. S., 1979, Ann. Rev. Astron. Astrophys., 17, 73
Sch"onell A. J., Storchi-Bergmann T., Riffel R. A., Riffel R., Bianchin M., Dahmer-Hahn L. G., Diniz M. R., Dametto N. Z., 2019, MNRAS, 485, 2054
Schnorr-Müller A., Storchi-Bergmann T., Nagar N. M., Ferrari F., 2014, MNRAS, 438, 3322
Schnorr-Müller A., Storchi-Bergmann T., Ferrari F., Nagar N. M., 2017, MNRAS, 466, 4370
Schoenmakers R. H. M., Franx M., de Zeeuw P. T., 1997, MNRAS, 292, 349
Scoville N. Z., Hall D. N. B., Ridgway S. T., Kleinmann S. G., 1982, ApJ, 253, 136
Sternberg A., Dalgarno A., 1989, ApJ, 338, 197
Storchi-Bergmann T., Schnorr-Müller A., 2019, Nature Astron., 3, 48
Storchi-Bergmann T., McGregor P. J., Riffel R. A., Simões Lopes R., Beck T., Dopita M., 2009, MNRAS, 394, 1148
Tody D., 1986, Instrumentation in astronomy VI, 627, 733
Tody D., 1993, Astronomical Data Analysis Software and Systems II, 52, 173
Turner J., Kirby-Docken K., Dalgarno A., 1977, ApJS, 35, 281
van de Ven G., Fathi K., 2010, ApJ, 723, 767
van den Bosch R. C. E., 2016, ApJ, 831, 134
Verheijen M. A. W., 2004, IAU Colloq. 195: Outskirts of Galaxy Clusters: Intense Life in the Suburbs, 394
Verheijen M. A. W., Zwaan M., 2001, Gas and Galaxy Evolution, 240, 867
Wenger M. et al., 2000, Astron. Astrophys. Suppl. Ser., 143, 9
Wilman R. J., Edge A. C., Johnstone R. M., 2005, MNRAS, 359, 755
Winge C., Riffel R. A., Storchi-Bergmann T., 2009, ApJS, 185, 186
Wolfinger K., Kilborn V. A., Koribalski B. S., Minchin R. F., Boyce P. J., Disney M. J., Lang R. H., Jordan C. A., 2013, MNRAS, 428, 1790
Wong T., Blitz L., Bosma A., 2004, ApJ, 605, 183
Young L. M., Bureau M., Cappellari M., 2008, ApJ, 676, 317

APPENDIX A: EXTINCTION AND GAS MASS DISTRIBUTION IN THE POLAR RING

From the colour map shown in Fig. 2, we have built the extinction map A_{F475W}–A_{F160W} shown in Fig. A1, for the inner 6 arcsec × 6 arcsec (440 × 440 pc^2) of NGC 4111, showing the reddening distribution along the dusty polar ring, calculated as described in Section 4.1. The spatial correlation with the H_2 λ2.1218 μm ring seen in the NIFS data is revealed by the overplotted white contours from the H_2 emission.

The second figure shown in this Appendix (Fig. A2) is a gas mass column density map of the same 6 arcsec × 6 arcsec (440 × 440 pc^2) region that covers the dusty polar ring. We again show in white, contours of the H_2 λ2.1218 μm line emission from NIFS data. This map has been obtained from the reddening map above following the steps discussed in Section 4.1. From this mass density map, integrating over the surface area of each spaxel, we obtained the cold gas mass as $M_{gas} = 9.8 \times 10^6$ M$_\odot$.

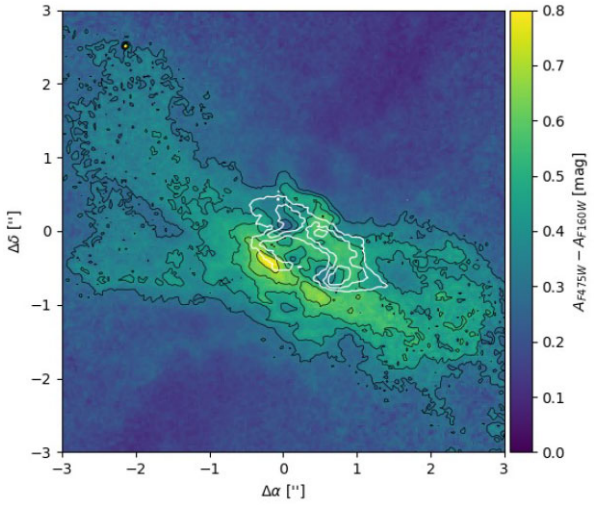

Figure A1. *HST* A_{F475W}-A_{F160W} map of the galaxy within the inner 6 arcsec × 6 arcsec (440 × 440 pc^2), that covers the dusty polar ring. Overplotted in white are the contours from the H_2λ2.1218 μm emission line flux distribution obtained from the NIFS data.

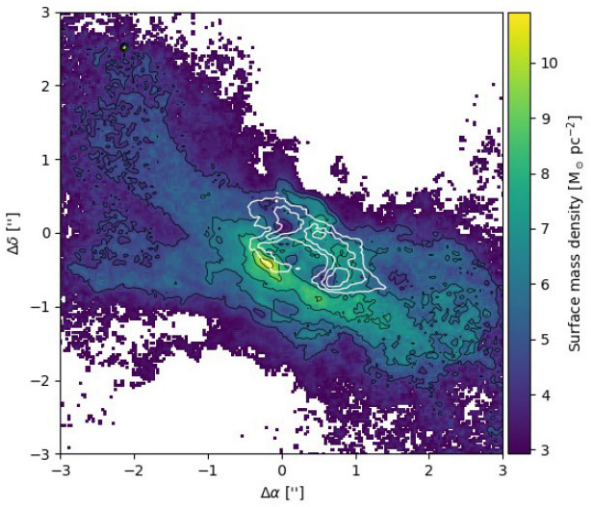

Figure A2. Gas mass column density map from the polar ring region obtained from the *HST* F475W–F160W colour map. Overplotted in white are the contours from the H_2λ2.1218 μm emission line flux distribution as derived from the NIFS data.

APPENDIX B: ERROR MAPS FROM THE NIFS KINEMATICS

In order to measure the intrinsic errors in the methods used for obtaining the NIFS stellar and molecular gas kinematics, we performed the Monte Carlo technique, perturbing the data with a Gaussian noise in every spaxel. From this, we obtained the error maps for the stellar and molecular gas kinematics, shown in Fig. B1. Similarly to Fig. 13, the top row shows the stellar kinematics errors and the bottom panels show those for the H_2 kinematics. From left to right, the panels show the error maps of the velocity v_{err}, velocity dispersion σ_{err}, and Gauss–Hermite moments $h_{3\,err}$ and $h_{4\,err}$. From these maps, we observe that the errors in the stellar kinematics decrease from the centre to the borders, while those for the H_2 gas kinematics do not vary much. The mean errors of each kinematic parameter (of the measurements shown in each map, not considering the masked spaxels) are listed in Table B1.

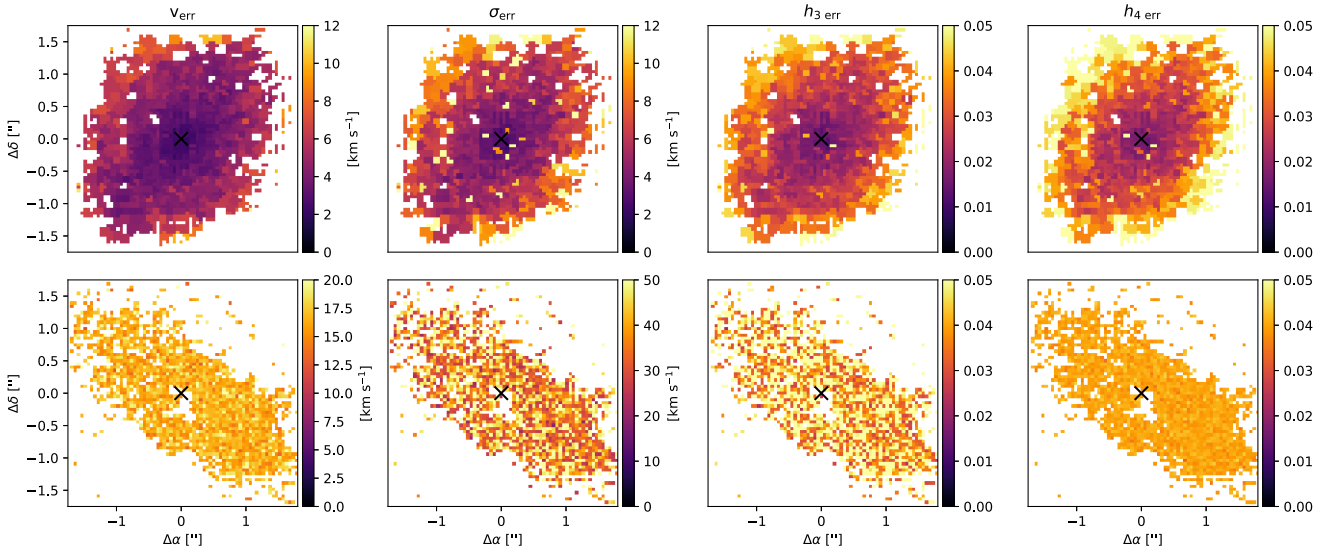

Figure B1. Monte Carlo error maps of the NIFS stellar (top panels) and molecular gas (bottom panels) kinematics fit. From left to right, the error maps of the velocity $v_{\rm err}$, velocity dispersion $\sigma_{\rm err}$ and Gauss–Hermite moments $h_{3\,\rm err}$ and $h_{4\,\rm err}$. The cross indicates the location of the galaxy nucleus.

Table B1. Mean Monte Carlo errors for each parameter of the NIFS stellar and molecular gas kinematics.

Parameter	Mean error Stars	Gas
$v_{\rm err}$	4.9 km s^{-1}	17.9 km s^{-1}
$\sigma_{\rm err}$	6.8 km s^{-1}	39.5 km s^{-1}
$h_{3\,\rm err}$	0.03	0.05
$h_{4\,\rm err}$	0.04	0.04

This paper has been typeset from a TEX/LATEX file prepared by the author.